

## INFORMATION TO USERS

This material was produced from a microfilm copy of the original document. While the most advanced technological means to photograph and reproduce this document have been used, the quality is heavily dependent upon the quality of the original submitted.

The following explanation of techniques is provided to help you understand markings or patterns which may appear on this reproduction.

1. The sign or "target" for pages apparently lacking from the document photographed is "Missing Page(s)". If it was possible to obtain the missing page(s) or section, they are spliced into the film along with adjacent pages. This may have necessitated cutting thru an image and duplicating adjacent pages to insure you complete continuity.
2. When an image on the film is obliterated with a large round black mark, it is an indication that the photographer suspected that the copy may have moved during exposure and thus cause a blurred image. You will find a good image of the page in the adjacent frame.
3. When a map, drawing or chart, etc., was part of the material being photographed the photographer followed a definite method in "sectioning" the material. It is customary to begin photoing at the upper left hand corner of a large sheet and to continue photoing from left to right in equal sections with a small overlap. If necessary, sectioning is continued again -- beginning below the first row and continuing on until complete.
4. The majority of users indicate that the textual content is of greatest value, however, a somewhat higher quality reproduction could be made from "photographs" if essential to the understanding of the dissertation. Silver prints of "photographs" may be ordered at additional charge by writing the Order Department, giving the catalog number, title, author and specific pages you wish reproduced.
5. PLEASE NOTE: Some pages may have indistinct print. Filmed as received.

**Xerox University Microfilms**

300 North Zeeb Road  
Ann Arbor, Michigan 48106

75-21,202

WAGNER, Kit Kern, 1947-  
INFLECTION POINT INSTABILITY WITHIN AN  
INVERSION LAYER.

The University of Oklahoma, Ph.D., 1975  
Physics, meteorology

**Xerox University Microfilms**, Ann Arbor, Michigan 48106

THIS DISSERTATION HAS BEEN MICROFILMED EXACTLY AS RECEIVED.

THE UNIVERSITY OF OKLAHOMA

GRADUATE COLLEGE

INFLECTION POINT INSTABILITY WITHIN AN INVERSION LAYER

A DISSERTATION

SUBMITTED TO THE GRADUATE FACULTY

in partial fulfillment of the requirements for the

degree of

DOCTOR OF PHILOSOPHY

BY

KIT KERN WAGNER

Norman, Oklahoma

1975

INFLECTION POINT INSTABILITY WITHIN AN INVERSION LAYER

APPROVED BY

\_\_\_\_\_  
*Jay S. Fern*  
\_\_\_\_\_  
*Clarence T. Gledhill*  
\_\_\_\_\_  
*John E. Francis*  
\_\_\_\_\_  
*Carl L. Hunn*

DISSERTATION COMMITTEE

## ABSTRACT

Three cases of the dissipation of nocturnally formed surface inversions were examined with the meteorological data from the National Severe Storms Laboratory tower. Two of the cases, 25 and 28 October 1971, exhibited different inversion behavior from the third. These two cases had large temperature fluctuations at the base of the inversion. The mean wind profile up to the inversion top was approximately an Ekman wind spiral. The third case, 21 October 1971, had much smaller temperature fluctuations in the inversion and the mean wind profile had little resemblance to an Ekman spiral.

The behavior of the height of the inversion base of these three cases was modeled numerically. Increased mixing over that caused by penetrative convection alone is required to account for the inversion behavior in the first two cases. The third case can be modeled with penetrative convection. Because of this it is thought some type of breaking wave instability is responsible for the large temperature fluctuations in the first two cases.

Based on the mean wind profile, the source of the breaking wave instability is sought in the inflection point instability of the Ekman wind profile. From the tower data a Reynolds number, a Richardson number, the approximate Ekman wind profile, and the orientation and wavelength of the temperature fluctuations were estimated. These provided input values to an infinitesimal perturbation model of the inflection point instability. With these input values, growing perturbations were

produced in the model. These perturbations occurred at a wavenumber of 0.44 on 25 October and 0.55 on 28 October and at an orientation of  $35^\circ$  to the left of the geostrophic wind.

It is thought this analysis shows the development of an Ekman wind profile under stable conditions; secondly, the creation of a less stable lower region by surface warming; and thirdly, the initiation of strong mixing at inversion base due to inflection point instability when the less stable air reaches the height of the inflection point in the wind profile. The intense mixing at inversion base causes the large observed temperature fluctuations.

#### ACKNOWLEDGMENTS

The author wishes to thank Dr. Y. Sasaki for his guidance of this research. Also my appreciation is extended to Dr. S. Barnes and Dr. R. Inman for their critical reading of the manuscript.

Recognition is given to Drs. Gersting and Jankowski for the computer program source listings which provided the basis for the modified version used in this study. Merrick Computing Center of the University of Oklahoma provided the computer services needed for the computations. I also wish to thank Ms. Anita Cameron for her help in the preparation of the manuscript.

The basic meteorological tower data set was provided by the National Severe Storms Laboratory. This cooperation is gratefully acknowledged.

This research was supported by the National Oceanic and Atmospheric Administration Grant No. 04-4-022-18.

TABLE OF CONTENTS

	Page
List of Tables . . . . .	vii
List of Illustrations . . . . .	viii
Chapter	
I. Introduction . . . . .	1
II. Observations from the Tower . . . . .	8
III. Model of Inversion Dissipation . . . . .	20
IV. Further Tower Observations . . . . .	29
V. The Ekman Layer Instabilities . . . . .	41
VI. The Inflection Point Instability Model . . . . .	45
VII. Comparison of the Data and the Model . . . . .	59
VIII. Conclusion . . . . .	62
References . . . . .	65
Appendix . . . . .	67

LIST OF TABLES

Table		Page
1.	Nomenclature . . . . .	5
2.	Heights of Instrumented Levels on NSSL Tower . . . . .	8
3.	Error of Model Inversion Base Height from Observed . . . . .	28
4.	Parameters of the Boundary Layer for 25 October 1971 . . . . .	33
5.	Parameters of the Boundary Layer for 28 October 1971 . . . . .	37
6.	Vertical Gradient of Potential Temperature and Mean Potential Temperature for the Layer. . . . .	38
7.	Aspect Ratio for Different Values of $\epsilon$ . . . . .	64

## LIST OF ILLUSTRATIONS

Illustration	Page
1. Coordinate Transformation . . . . .	3
2. Temperature Time Series, 25 October 1971. . . . .	10
3. Vertical Profile of Wind Speed, 25 October 1971 . . .	12
4. Temperature Time Series, 28 October 1971 . . . . .	14
5. Vertical Profile of Wind Speed, 28 October 1971 . . .	15
6. Vertical Profile of Wind Speed, 21 October 1971 . . .	17
7. Temperature Time Series, 21 October 1971. . . . .	18
8. Schematic of Inversion Dissipation Model. . . . .	21
9. Development of a Kelvin-Helmholtz billow. . . . .	25
10. Behavior of Inversion Base Height . . . . .	26
11. Hodographs, 25 October 1971 . . . . .	30
12. Component Wind Speeds, 0800 CST, 25 October 1971. . .	32
13. Hodographs, 28 October 1971 . . . . .	34
14. Component Wind Speeds, 0730 CST, 28 October 1971. . .	36
15. Values of Growth Rate in the $\epsilon$ and $\alpha^*$ Domain. . . . .	61

# INFLECTION POINT INSTABILITY WITHIN AN INVERSION LAYER

## CHAPTER I

### INTRODUCTION

Three cases of the morning dissipation of nocturnally formed inversions are examined using data from the National Severe Storms Laboratory meteorological tower. Large temperature fluctuations during the inversion dissipation appear in the time series data of two of the cases, 25 and 28 October 1971. These fluctuations were in the lower portion of the shallow inversion layer. The third case, 21 October 1971, had temperature fluctuations which were much smaller in magnitude. Increased turbulent mixing at the inversion base is thought to be the cause of the large temperature fluctuations.

The factors contributing to the inversion dissipation are examined with a horizontally homogeneous model of inversion behavior. Convective penetration is considered with a model similar to those of Tennekes (1973) and Carson (1973). Enhanced turbulent mixing at the inversion base, such as might be generated by wind shear instability, is also considered. The model is modified to include this by using a finite depth for the mixing region instead of an infinitesimal depth. The comparison of the models, with and without increased mixing at inversion base, shows that increased mixing occurs for the first two cases.

The observed wind profiles suggest shear instability is likely

in the inversion region. Up to the top of the inversion, the vertical profile of horizontal wind approximated the Ekman spiral solution to the boundary layer equations. At the inversion top the wind speed reached a local maximum. A possible mechanism to initiate the turbulent fluctuations is sought in the inflection point instability of a stratified Ekman boundary layer. Brown (1970) has applied this mechanism to the explanation of the horizontal roll vortices that are observed in the atmospheric boundary layer. Their scale is a horizontal wavelength of one to five kilometers and a characteristic depth of 500 to 3500 meters. However, a scale analysis of the boundary layer equations shows the mechanism of inflection point instability might be applicable to a wider range of boundary layer phenomena, particularly those of restricted vertical extent.

The observed instability is thought to be the incipient stage of this dynamic instability that has been considered as a mechanism for the horizontal roll vortices in the planetary boundary layer (Brown, 1972a; LeMone, 1973). The structure of the instability is assumed to occur as a two-dimensional disturbance in a y-z plane (see Table 1 for an explanation of symbols). The y coordinate is the lateral horizontal axis and z is the vertical coordinate. The atmospheric perturbation state is considered to be uniform in the direction of the longitudinal axis, x. This direction of uniformity is at an angle from the geostrophic wind direction above the boundary layer. Fig. 1 shows how the x axis is rotated an angle  $\epsilon$  from the geostrophic wind,  $\vec{V}_g$ .

An examination of the observed tower data assesses the compatibility of the inflection point instability model with the observations.

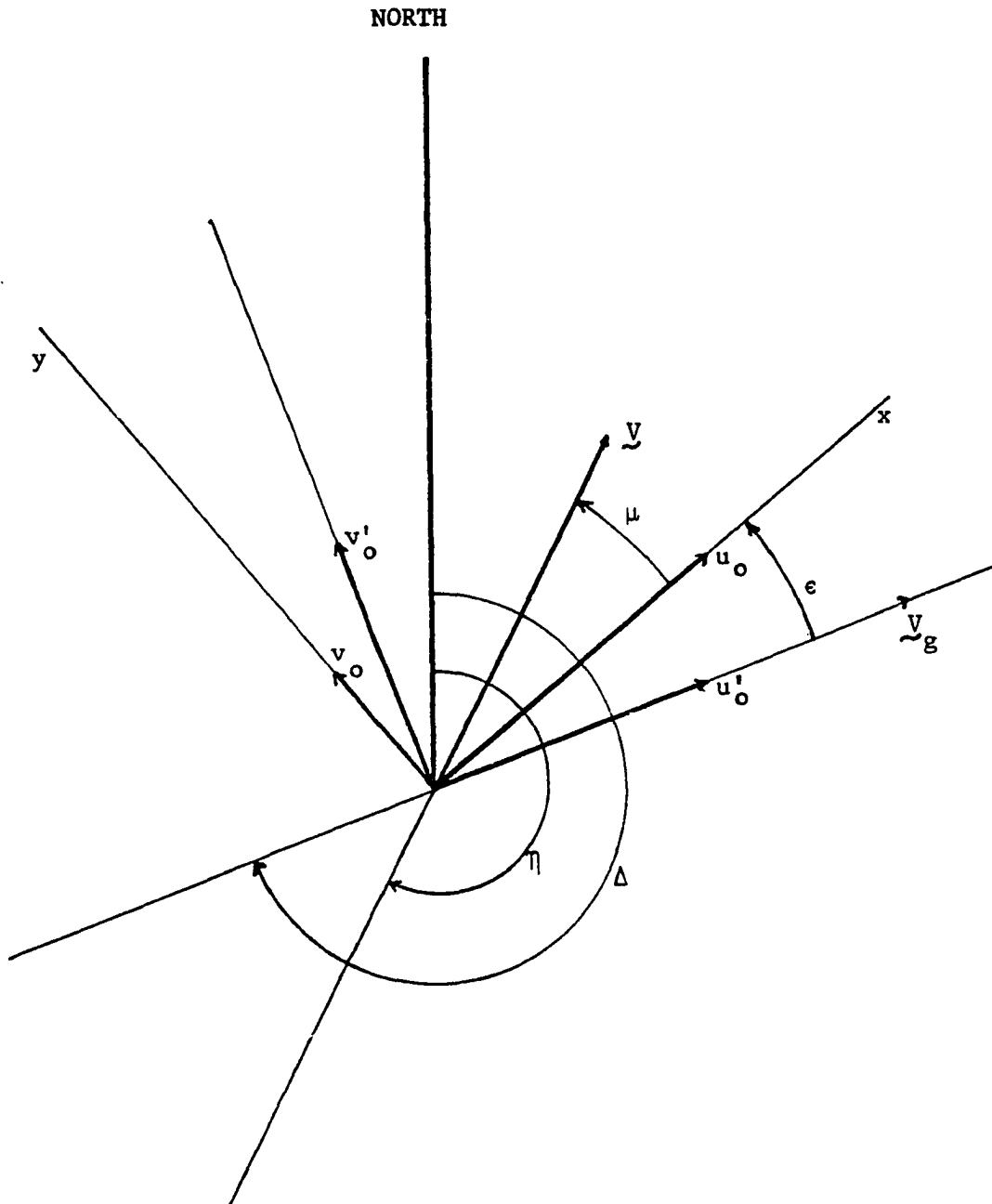


Figure 1. Transformation from the coordinates along and perpendicular to the geostrophic wind to the coordinates of the disturbance. The disturbance is oriented at an angle  $\epsilon$  counter-clockwise from  $\tilde{V}_g$ . In the disturbance coordinates,  $u_o = V \cos \mu$ ,  $v_o = \tilde{V}^g \sin \mu$ , where  $\mu = \Delta - \epsilon - \eta$ .

It shows the observed mean wind and temperature profiles are in excellent agreement with the stratified Ekman layer model. To explain the temperature fluctuations, a linear infinitesimal perturbation model of the inflection point instability is used. The model is formulated as an eigenvalue problem where the structure of the boundary layer specifies the coefficients of the equation. The eigenvalue is the growth rate of the infinitesimal perturbations. Because the growth rate is the indicator of stability in the model, a search is made for the largest growth rate. The angle  $\epsilon$  is an important parameter in determining where the largest growth rate occurs. However,  $\epsilon$  is not available from the tower data. The technique used in this study is to specify many values of  $\epsilon$  and observe for each value how well the model compares to the known locations of maximum growth rate. The results indicate instability for input parameters derived from the tower measurements. Thus the inflection point instability of a stratified Ekman layer is accepted as a possible source of the turbulent mixing causing the temperature fluctuations.

TABLE 1

## NOMENCLATURE

A	Convective layer of boundary layer.
$\underline{A}$	Coefficient matrix of linear boundary value equation.
B	Mixing layer between convective layer and inversion layer.
$\underline{B}$	Coefficient matrix of inner boundary conditions.
$b_1, b_2, \dots$	Coefficients of boundary condition equations.
C	Inversion layer.
$C_1, C_2$	Coefficients of heat flux terms.
$C_p$	Specific heat capacity of air at constant pressure.
CST	Central Standard Time.
$c, c_r, c_i$	Phase velocity; complex, real, imaginary.
$c_1, c_2, \dots$	Coefficients of the 6th order differential equation.
$\underline{D}$	Coefficient matrix of outer boundary conditions.
f	Coriolis parameter.
f(c)	Function of phase velocity.
$g, g_0$	Gravity; dimensional, non-dimensional
H	Vertical length scale.
H'	Non-dimensional height of boundary layer model.
h	Height of inversion base above surface.
i	$\sqrt{-1}$
K	Degrees Kelvin.
$K_h$	Eddy coefficient of turbulent heat exchange.
$K_m$	Eddy coefficient of turbulent momentum exchange.
k	Number of boundary conditions at inner boundary.
L	Horizontal length scale.
n	Order of linear boundary value equation.
P	Reference atmospheric pressure.
Pr	Prandtl number.
p	Actual atmospheric pressure.
q	Frequency.

TABLE 1 (continued)

R	Gas constant of dry air.
Re	Reynolds number.
$Ri_b, Ri_l$	Richardson number; bulk, local.
Ro	Rossby number.
T	Air temperature.
t	Time coordinate.
t*	Time scale of breaking wave.
u	x component of wind.
$u_o$	x component of wind in disturbance coordinates.
$u'_o$	Component of wind in the direction of $\underline{V}_g$ .
$\underline{V}, V$	Actual wind; vector, magnitude.
$\underline{V}_g, V_g$	Geostrophic wind; vector, magnitude.
$v_{ip}$	$v_o$ at the inflection point.
$\partial V / \partial z_{ip}$	Vertical shear of $v_o$ at the inflection point.
v	y component of wind.
$v_o$	y component of wind in disturbance coordinates.
$v'_o$	Component of wind in the direction perpendicular to $\underline{V}_g$ .
$\underline{W}$	Magnitude of $\underline{\Phi}$ .
w	z component of wind.
$\underline{X}$	Orthogonalized $\underline{\Phi}$ .
x	Longitudinal horizontal coordinate axis.
$\underline{Y}$	Matrix of $\varphi$ and its derivatives.
y	Lateral horizontal coordinate axis.
$y_1, y_2, y_{1(1)} \dots$	Elements of matrix $\underline{Y}$ .
$\underline{Z}$	Orthonormalized $\underline{\Phi}$ .
$Z_{ip}$	Height of inflection point.
z	Vertical coordinate axis.
$\alpha, \alpha^*$	Wavenumber.
$\beta$	Subsidence parameter.
$\beta_1, \beta_2, \dots$	Superposition coefficients.
$\gamma$	Lapse rate of potential temperature.
$\gamma'$	Orthogonalization criteria angle.

TABLE 1 (continued)

$\Delta$	Direction of geostrophic wind.
$\Delta h$	Thickness of inversion interfacial mixing layer.
$\Delta\theta$	Inversion strength.
$\delta$	Ekman depth.
$\epsilon$	Orientation angle from $\underline{y}_g$ .
$\eta$	Direction of actual wind.
$\Theta$	Potential temperature of convective layer.
$\Theta^*$	Observed potential temperature of convective layer.
$\bar{\Theta}$	Reference temperature.
$\theta$	Potential temperature.
$\theta_c$	Potential temperature of inversion layer.
$\theta_o$	Reference potential temperature.
$\lambda$	Wavelength.
$\mu$	Angle between x axis and V.
$\Pi$	Non-dimensional pressure parameter.
$\pi$	Pi.
$\rho, \rho_m, \rho_o$	Air density.
$\bar{\rho}$	Reference air density.
$\tau$	Amplitude of temperature perturbation.
$\Phi$	Matrix of $\varphi$ and its derivatives.
$\varphi$	Amplitude of streamfunction perturbation.
$\chi$	Aspect ratio.
$\psi$	Streamfunction.

## CHAPTER II

### OBSERVATIONS FROM THE TOWER

The National Severe Storms Laboratory meteorological tower facility is on the WKY-TV television transmitting tower. The tower is on the northern side of Oklahoma City, Oklahoma amid a rural area of slightly rolling terrain. In 1971, seven levels were instrumented. Table 2 gives the height above ground for each of these levels.

TABLE 2  
HEIGHTS OF INSTRUMENTED LEVELS ON NSSL TOWER

<u>Level</u>	<u>Height (meters)</u>
0	26.0
1	43.7
2	89.5
3	176.3
4	265.5
5	355.6
6	443.8

The instruments on the tower are mounted on booms which extend to the southwest. For this study, wind and temperature measurements were recorded by a digital system and made available for study in the form of magnetic tape. Complete descriptions of the tower site and instrumentation are given by Sanders and Weber (1970) and Carter (1970).

The wind and temperature features observed on the tower during the mornings of 25 and 28 October 1971 were very similar. A nocturnal inversion of several hundred meters depth was present at sunrise. Subsequently both the base and the top of the inversion layer move upward

with time, finally passing above the tower top. At sunrise the wind profile through much of the tower layer has the approximate shape of an Ekman wind spiral. Near the inversion top, the wind speed reached its maximum value. During the time the inversion was rising, the wind profile changed such that this wind speed maximum remained coincident with the inversion top.

On 21 October 1971 the wind and temperature are somewhat different. The inversion persists at the lower levels of the tower for an hour longer than on 25 and 28 October. The wind speed is about half that of the other two cases and the profile has little resemblance to the Ekman spiral. There is a speed maximum in the profile that is coincident with the inversion top, however.

The temperature structure and the behavior of the inversion for each of the three cases will now be examined. The differences and similarities between them will point out the anomaly of the large temperature fluctuations.

The synoptic situation for 25 October 1971 has a cold front moving from the Colorado-New Mexico area, becoming stationary in the Texas-Oklahoma panhandles by midday. To the east a surface high pressure ridge extended north from Louisiana to the Great Lakes causing southerly winds over Oklahoma. Scattered cirrus during the morning increased in extent through the day.

Before sunrise, about 0645 CST on 25 October 1971, an inversion extended from the surface to between levels 4 and 5 of the tower. The time history of this inversion is shown in Fig. 2. The dots indicate the beginning and end of inversion lapse rates between the tower levels.

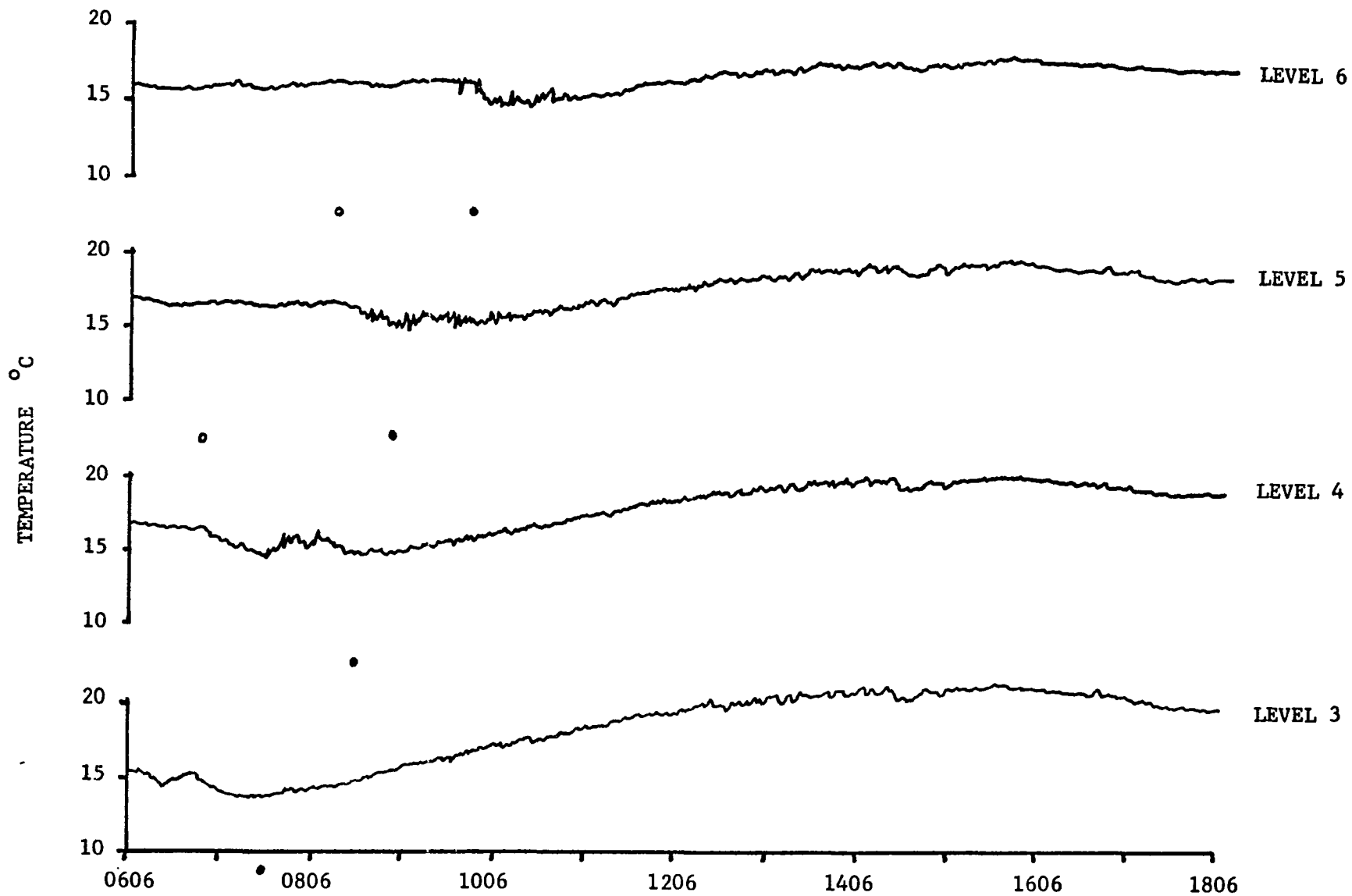


Figure 2. Time series of temperature 25 October 1971. The  $\circ$  indicate the beginning and the  $\bullet$  indicate the end of an inversion lapse rate between the tower levels.

The inversion base had lifted from the surface by 0730 CST, while the inversion top had moved above the top of the tower by 0855 CST. Also before sunrise there was a low-level wind speed maximum at level 4. Fig. 3 shows this and the temporal changes of the vertical profile of horizontal wind speed. The low-level wind maximum moved upward in such a manner as to stay coincident with the inversion top. Blackadar (1957) showed this to be a necessary condition if the inversion is to avoid chaotic dissipation.

Anomalous temperature fluctuations appear in the level 4 temperature time series starting at 0730 CST. They continued at this level until 0830 CST. Fig. 2 shows these temperature time series at levels 3 to 6 for 0606-1806 CST. The large fluctuations, for the most part, appear at only one level at a time and move upward with the inversion. The trough to crest amplitude of the fluctuations is approximately 1 K, which is much larger than the temperature fluctuations at the other levels at the same time. The appearance of these anomalous fluctuations is very different from the fluctuations associated with the convective activity of the afternoon.

The inversion top passed above level 5 at approximately 0740 CST and level 6 at 0900 CST. The inversion base passed level 4 at 0910 CST, level 5 at 0940 CST, and level 6 at 1010 CST. A comparison with the temperature fluctuation occurrence shows the temperature fluctuations are near the inversion base. At level 4 the fluctuations exist from 0730-0840 CST, at level 5 from 0830-1015 CST, and at level 6 from 0940-1050 CST. Following the rise of the inversion base above the tower top at 1010 CST, the temperature begins the normal diurnal variation. Convective temperature

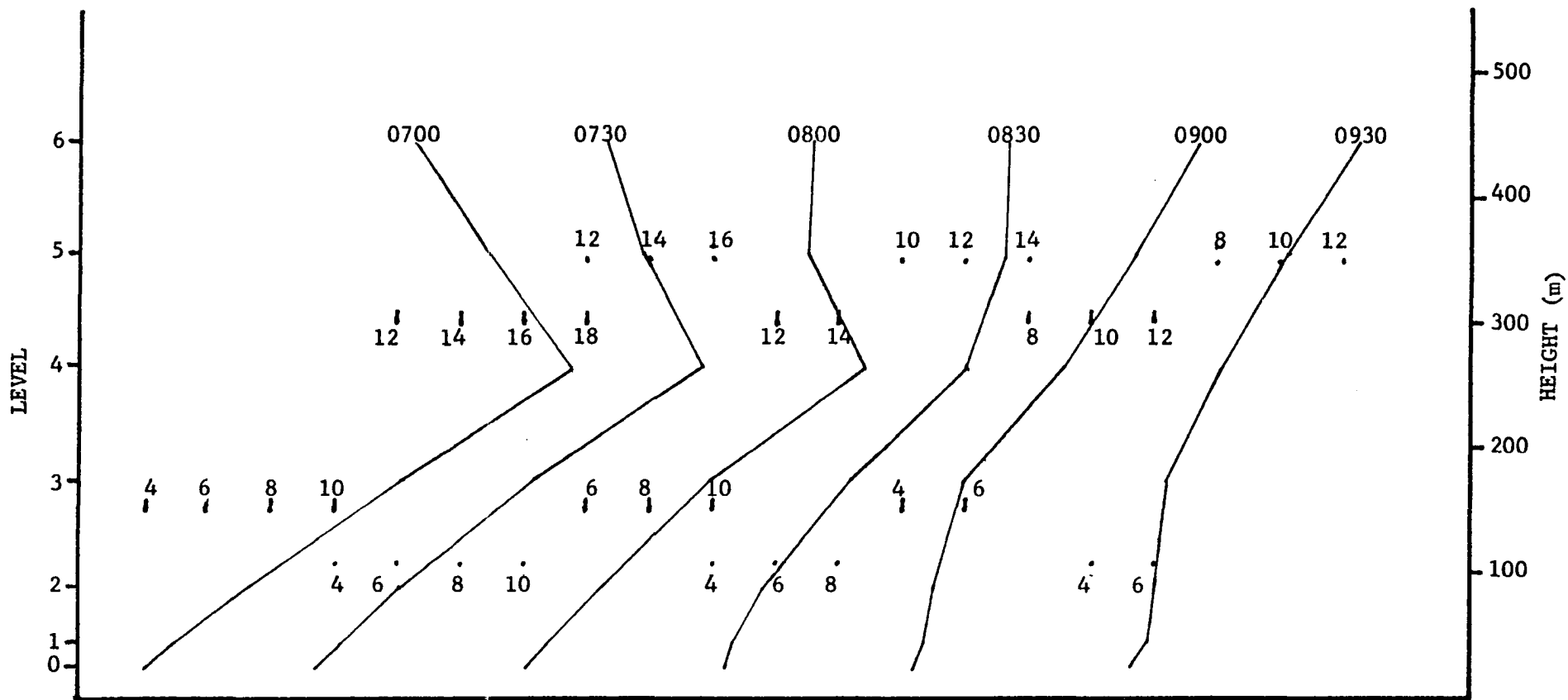


Figure 3. Vertical profile of horizontal wind speed for the times indicated on 25 October 1971. Wind speeds are in  $\text{m s}^{-1}$ .

fluctuations appear at all levels after 1230 CST and last throughout the afternoon.

The time series of wind speed show that turbulence developed in the horizontal wind at approximately the same time the temperature fluctuations began. At the upper levels the horizontal wind was nearly laminar until the inversion base rose up to these levels. The turbulence in the wind speed continues until the evening.

The tower data of 28 October 1971 will now be discussed to show that the same general features were present in the boundary layer on that date as on the 25th. The morning of 28 October 1971 finds a stationary front extending from Colorado across Kansas to Missouri. Surface winds over Oklahoma were from the southeast bringing considerable moisture from the Gulf of Mexico. Fog was observed over the central Oklahoma area until 1200 CST. Due to this, vigorous convective activity was retarded until the afternoon, much later than that on 25 October.

Fig. 4 shows the progression of the inversion through the tower layer. Its rate of rise is only slightly slower than the inversion on the 25th. However, the transition period from inversion to superadiabatic is three to four hours, compared to one to two hours on 25 October. As on 25 October, at sunrise the inversion top is slightly above level 4. The wind speed maximum at level 4 is not quite as intense as on the 25th, but still is coincident with the inversion top. The inversion top moves upward, passing level 5 at 0830 CST and the tower top at 0930 CST. The vertical profiles of horizontal wind speed, Fig. 5, show how the wind speed maximum rises at the same rate as the inversion.

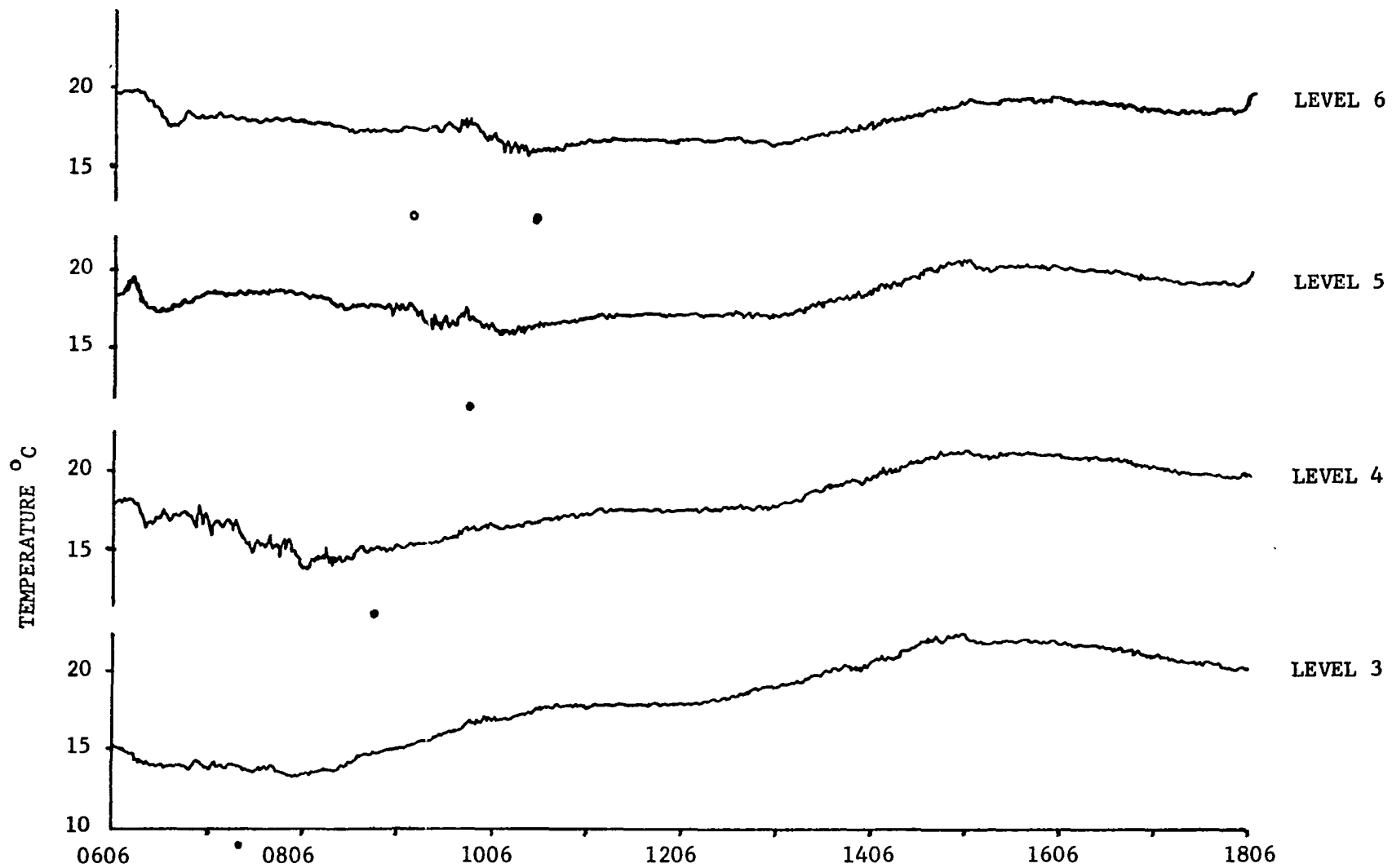


Figure 4. Time series of temperature 28 October 1971. The  $\circ$  indicate the beginning and the  $\bullet$  indicate the end of an inversion lapse rate between the tower levels.

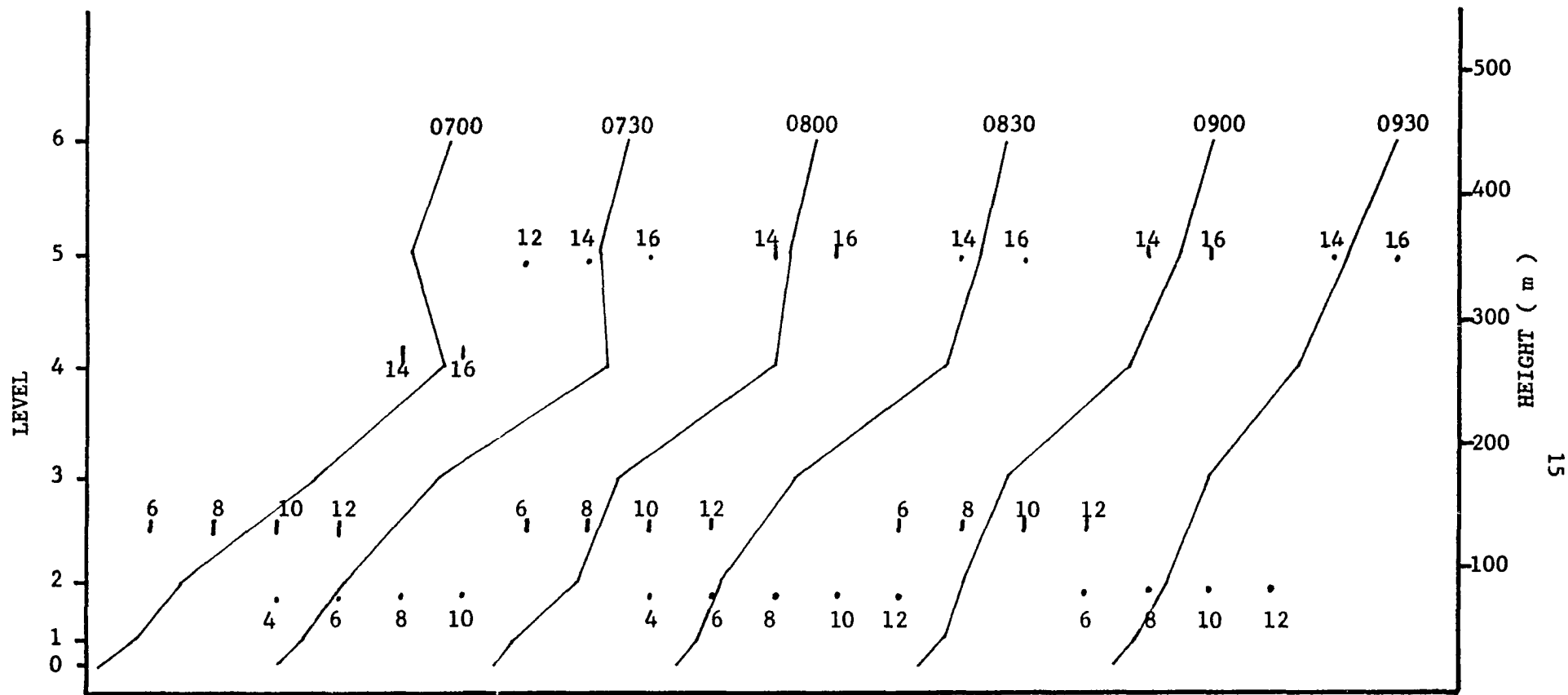


Figure 5. Vertical profile of horizontal wind speed for times indicated on 28 October 1971.  
Wind speed is in  $\text{m s}^{-1}$ .

The anomalous temperature fluctuations again begin at level 4. Their initial appearance is at 0620 CST and the fluctuations continue at this level until 0800 CST. Fig. 4 is the 28 October time series of temperature for levels 3 to 6. The presence of the large temperature fluctuations is revealed at level 5 from 0900 to 1010 CST and at level 6 from 0915 to 1025 CST. A comparison with the location of inversion base shows again the fluctuations occur slightly above the inversion base.

Laminar flow in the horizontal wind is present at the upper levels on 28 October as it was on 25 October. At the time the fluctuations are initiated in the temperature time series the horizontal wind becomes turbulent.

On 21 October a high pressure area between two frontal systems was over the plains. To the west a cold front extending from Wyoming to California moved into Oklahoma the following day. To the east a cold front was present from a low in Iowa to western Louisiana. Surface winds in Oklahoma in the morning were from the northwest under clear skies. Afternoon cumulus developed later.

The inversion on 21 October was somewhat shallower than those on 25 and 28 October. The top of the inversion at sunrise was between levels 2 and 3. A small wind speed maximum, seen in Fig. 6, is coincident with the inversion top. The progress of the inversion dissipation at levels 3 and 4 is about one hour behind that on 25 and 28 October. The inversion top passes level 4 at 0823 CST, level 5 at 0844 CST and the tower top at 0936 CST. Fig. 7 shows when the inversion lapse rate began and ended between the tower levels. Despite the late start the inversion passes above the tower five to twenty minutes later than on 28 and

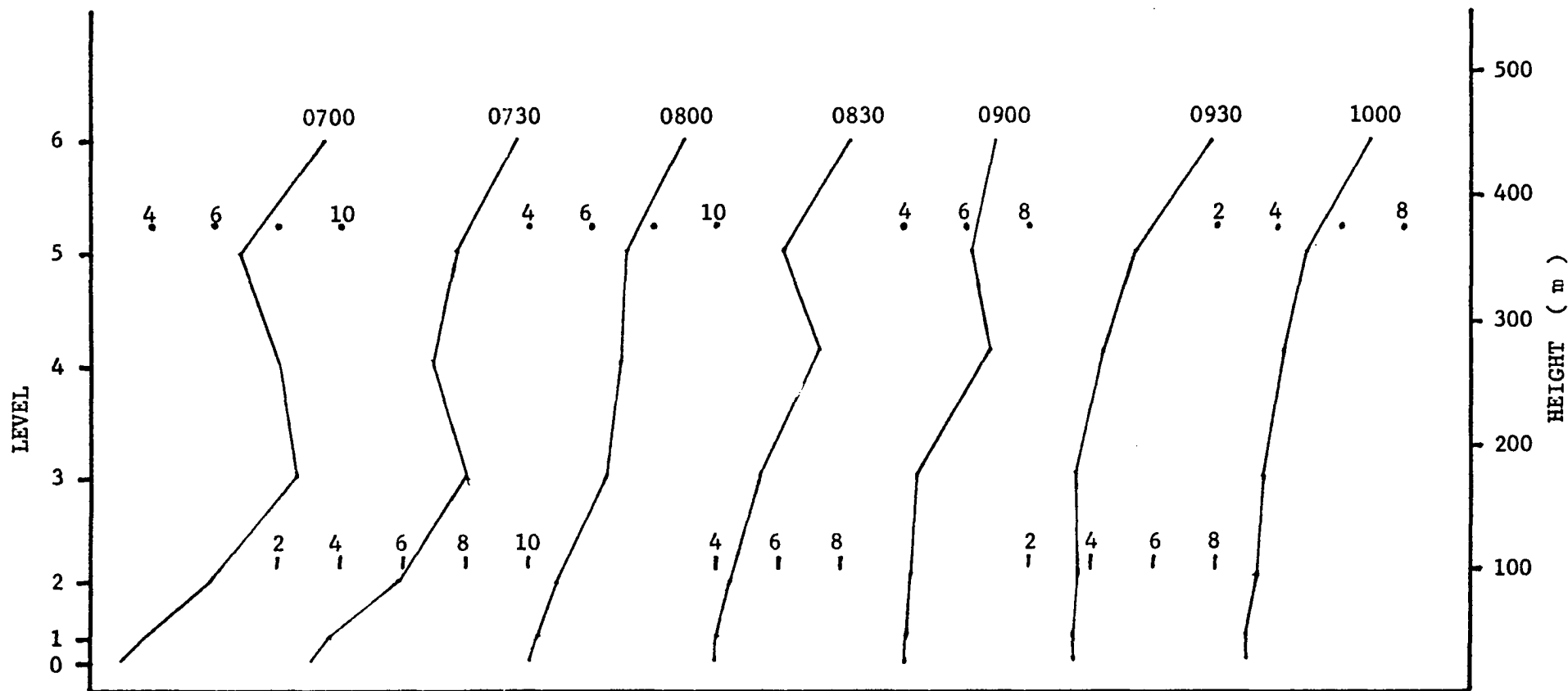


Figure 6. Vertical profile of horizontal wind speed for times indicated on 21 October 1971.

Wind speed is in  $\text{m s}^{-1}$ .

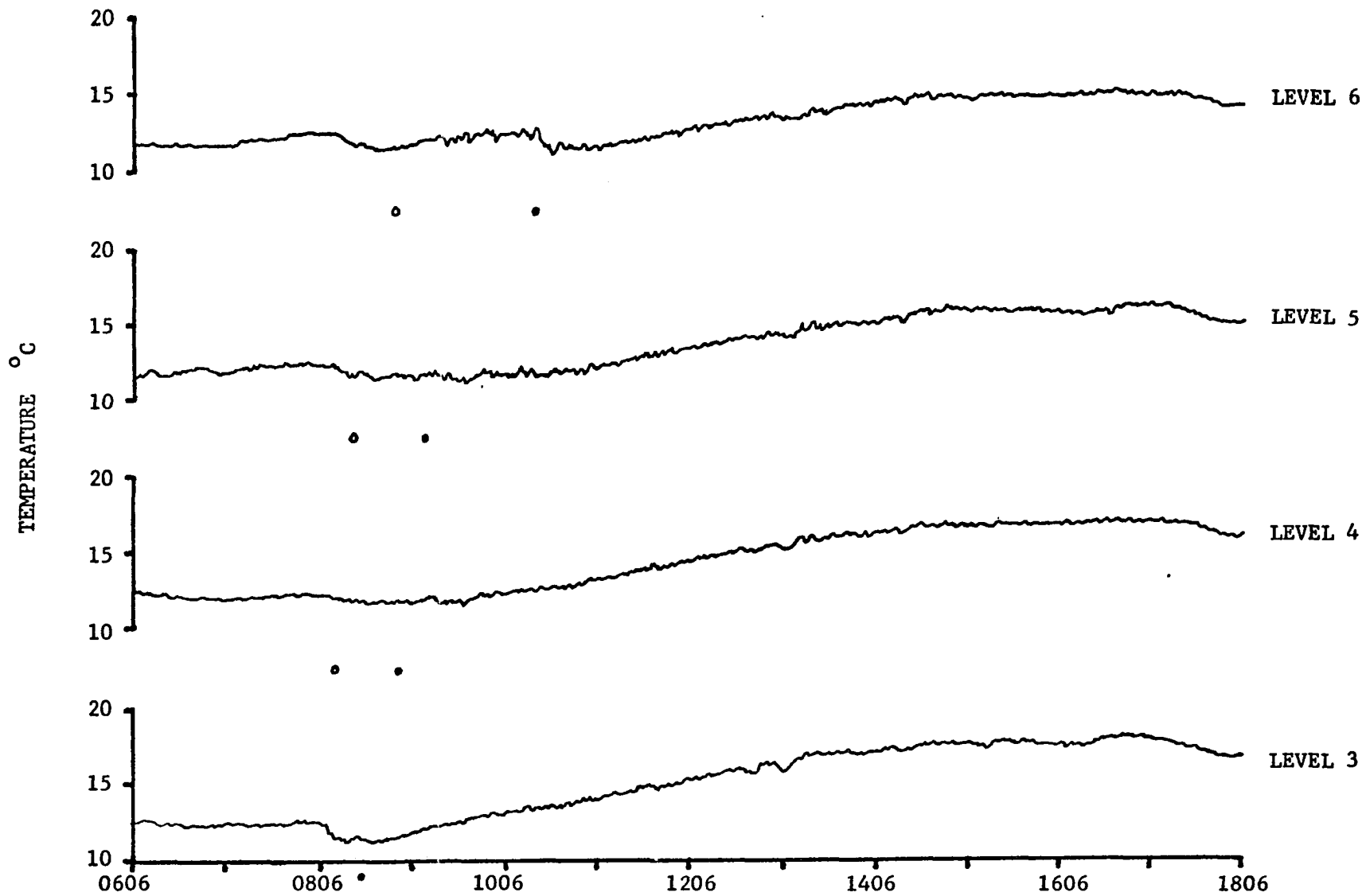


Figure 7. Time series of temperature 21 October 1971. The o indicate the beginning and the • indicate the end of an inversion lapse rate between the tower levels.

25 October. It is in the early hours when the rate of inversion rise has a different behavior from 25 and 28 October.

Fig. 7 also shows the time series of temperature on 21 October. The morning hour fluctuations at levels 4 and 5 are about 0.2 K in magnitude. Level 6 does show some larger fluctuations occurring near inversion base, but not quite the degree seen on 25 and 28 October.

This comparison of the temperature time series of the three cases shows the magnitude of the temperature fluctuations at inversion base for 25 and 28 October to be about five times the magnitude of those on 21 October. One possible source of the fluctuations is the vertical motions caused by penetrative convection into the stable inversion layer. Laboratory investigations of penetrative convection by Deardorff, Willis, and Lilly (1969) have observed temperature fluctuations at the inversion interface. Undoubtedly this is occurring to some extent in the cases of this study. It is not known if penetrative convection alone could be responsible for the large magnitude of the temperature fluctuations seen in two of the cases.

Another possible source of turbulent vertical motions, which can produce temperature fluctuations at the inversion base, is breaking waves generated by wind shear instability. This phenomenon has been observed by remote sensing instruments, e.g., Emmanuel *et al.* (1972). The relative contributions of penetrative convection, breaking waves, and other factors is examined in the next section. Further study of the tower data will come in Chapter IV.

## CHAPTER III

### MODEL OF INVERSION DISSIPATION

The contributions of the various factors to inversion dissipation are determined by inputting data from the tower measurements into a model of inversion behavior. The relative contributions of penetrative convection and a parameterized breaking wave are found by adjusting their influence in the model until the observed inversion behavior is predicted by the model.

This model of an inversion in the planetary boundary layer first assumes horizontal homogeneity. Horizontal advection is ignored. The model consists of three layers. These are shown in Fig. 8. In the lowest layer, A, turbulent convection occurs. The layer has a potential temperature,  $\Theta$ , which is independent of  $z$ . The layer extends from the surface to the base of the inversion layer at height  $h$ . The top layer, C, has an inversion lapse rate. It is assumed to be free of turbulent motions. The gradient of potential temperature,  $\gamma$ , in this layer is a function of the large scale vertical motion. The potential temperature of layer C is defined as

$$\theta_c(z,t) = \theta_o + \gamma(t)z. \quad (1)$$

Between C and A is layer B. In this layer of thickness  $\Delta h$  the warmer air of the inversion layer is entrained into the convective layer. A temperature discontinuity exists between  $\Theta$  and  $\theta_c$ . This discontinuity

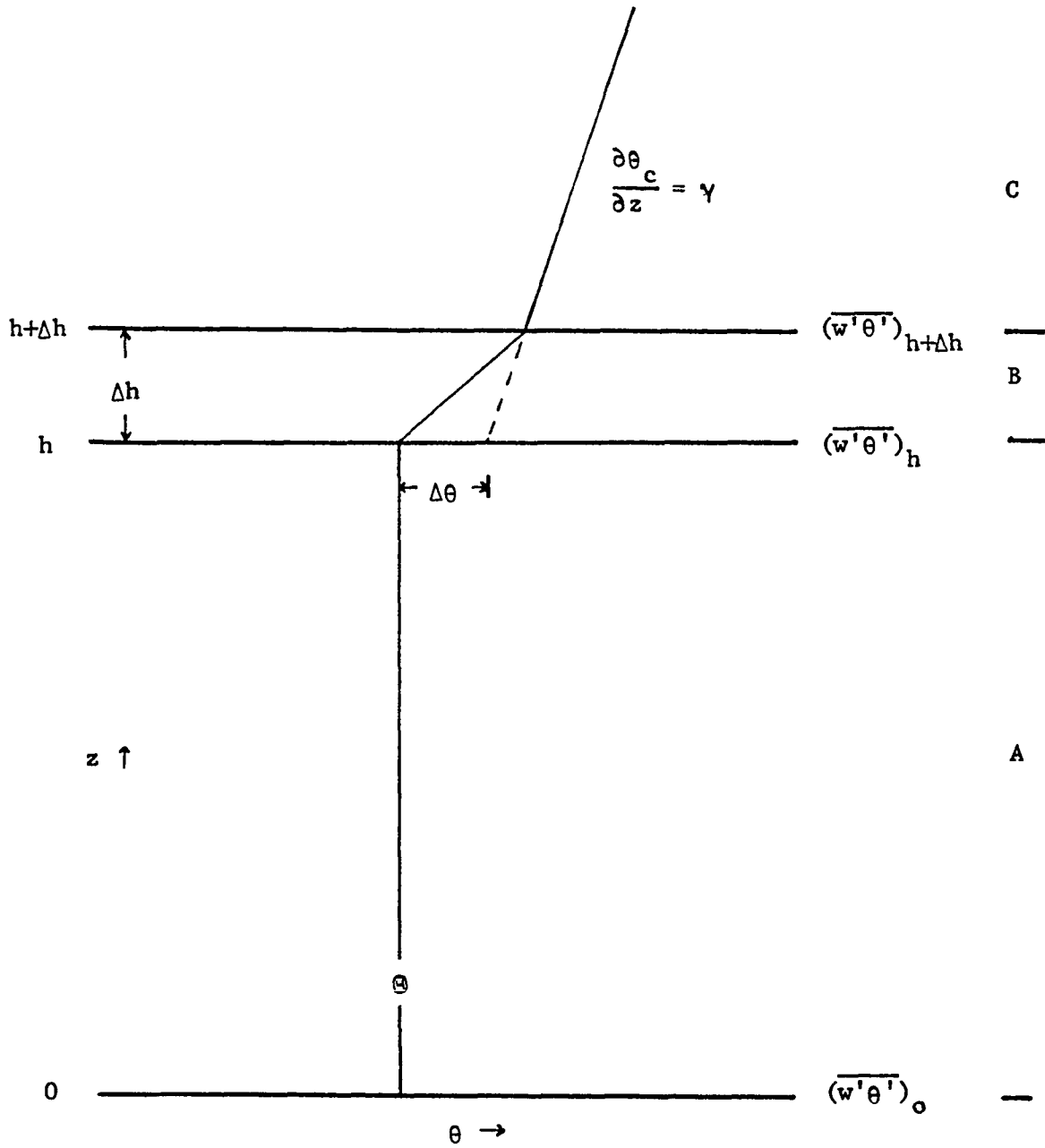


Figure 8. Schematic of the inversion dissipation model. Layer A is the convective region. Layer B is the turbulent interfacial mixing region. Layer C is the stable inversion layer.

defines the inversion strength,  $\Delta\theta$ , where

$$\Delta\theta = \theta_c(h + \Delta h, t) - \gamma\Delta h - \Theta. \quad (2)$$

Previous models of inversion dynamics, such as Tennekes (1973), Carson (1973) and Betts (1973) have assumed  $\Delta h$  to be zero. This has produced a satisfactory model of penetrative convection, but it leaves no way to model the breaking wave effect. Betts (1974) has stated parts of a model with finite  $\Delta h$ . It has not been fully developed, however.

The model herein is developed with an energy budget for each of the three layers. In layer C the energy equation becomes

$$\frac{\partial\theta_c}{\partial t} + w(z) \frac{\partial\theta_c}{\partial z} = 0. \quad (3)$$

By substituting (1) into (3) it can be seen that

$$w = -\frac{1}{\gamma} \frac{\partial\gamma}{\partial t} z = -\beta z, \quad (4)$$

and

$$\gamma = \gamma(0) \exp \beta t. \quad (5)$$

$\beta$  is referred to as the subsidence parameter and is determined from observations of the large scale vertical motion,  $w$ .

For layer B the vertical turbulent transports are considered to be much larger than the large-scale vertical motion. In this case the energy budget is

$$\frac{\partial\theta}{\partial t} = -\frac{\partial}{\partial z} (\overline{w'\theta'}), \quad (6)$$

where  $\overline{w'\theta'}$  is the turbulent transport term averaged over some time interval. This equation is integrated from  $h$  to  $h + \Delta h$ , i.e.,

$$\begin{aligned} \frac{1}{\Delta h} \int_h^{h+\Delta h} \frac{\partial \theta}{\partial t} dz &= \frac{d}{dt} \frac{1}{\Delta h} \int_h^{h+\Delta h} \theta dz + \frac{1}{(\Delta h)^2} \int_h^{h+\Delta h} \theta dz \frac{d\Delta h}{dt} \\ &- \frac{\theta_{h+\Delta h}}{\Delta h} \frac{d(h+\Delta h)}{dt} + \frac{\theta_h}{\Delta h} \frac{dh}{dt} = - \frac{1}{\Delta h} \int_h^{h+\Delta h} \frac{\partial}{\partial z} (\overline{w'\theta'}) dz. \end{aligned} \quad (7)$$

The middle terms of (7) follow from applying Leibnitz' rule. Substituting for

$$\frac{1}{\Delta h} \int_h^{h+\Delta h} \theta dz$$

an average of  $\theta_{h+\Delta h}$  and  $\theta_h$  and assuming  $\Delta h$  is constant, (7) is integrated to

$$\begin{aligned} \frac{1}{2} \frac{d}{dt} (\theta_{h+\Delta h} + \theta) - \frac{1}{\Delta h} \frac{dh}{dt} (\theta_{h+\Delta h} - \theta) &= - \frac{1}{\Delta h} [(\overline{w'\theta'})_{h+\Delta h} \\ &- (\overline{w'\theta'})_h]. \end{aligned} \quad (8)$$

$(\overline{w'\theta'})_{h+\Delta h}$  is zero because the model assumes there is no turbulent transport of heat into layer C. With (1) and (2), (8) becomes

$$\frac{1}{2} \frac{d}{dt} [\gamma(h+\Delta h) + \theta] - \frac{1}{\Delta h} \frac{dh}{dt} (\Delta\theta + \gamma\Delta h) = \frac{1}{\Delta h} (\overline{w'\theta'})_h \quad (9)$$

or

$$\frac{\Delta h}{2} \left[ (h+\Delta h) \beta \gamma + \frac{d\theta}{dt} \right] - (\Delta\theta + \frac{\gamma\Delta h}{2}) \frac{dh}{dt} = (\overline{w'\theta'})_h. \quad (10)$$

An additional equation is derived by differentiating the definition of  $\Delta\theta$ , i.e.,

$$\frac{d\Delta\theta}{dt} = \frac{d}{dt} [\gamma(h+\Delta h) - \gamma\Delta h - \theta] = \gamma \frac{dh}{dt} + h\beta\gamma - \frac{d\theta}{dt}. \quad (11)$$

Layer A is also assumed to be dominated by vertical turbulent transports so that (6) is the energy budget for this layer. Tower

measurements of flux were made at 45 m. Because of this, layer A is divided into two regions and each is integrated separately. The energy budget for the region from  $45 \text{ m} < z < h$  is

$$(h-45) \frac{\partial \Theta}{\partial t} = \overline{(w'\theta')}_{45} - \overline{(w'\theta')}_h, \quad (12)$$

and from  $0 < z < 45 \text{ m}$  is

$$45 \frac{\partial \Theta^*}{\partial t} = \overline{(w'\theta')}_0 - \overline{(w'\theta')}_{45}, \quad (13)$$

where  $\Theta$  and  $\Theta^*$  are the mean temperatures of the layers and assumed independent of  $z$ .

Penetrative convection has been parameterized by previous investigators (Tennekes, 1973; Carson, 1973; Betts, 1973) by assuming that the turbulent transport across the inversion base is some negative fraction of the surface heat flux, i.e.,

$$-\overline{(w'\theta')}_h = C_1 \overline{(w'\theta')}_0. \quad (14)$$

The sign is negative since the warmer air above is being entrained into the cooler air below. Tennekes (1974) and Carson (1973) have found empirically that  $C_1$  is about 0.5.

The complete model for penetrative convection effects only, is (10), (11), (12), (13), and (14). The unknowns are  $\Theta$ ,  $\Delta\theta$ ,  $h$ ,  $\overline{(w'\theta')}_0$  and  $\overline{(w'\theta')}_h$ . For penetrative convection  $\Delta h$  is set to zero. The parameters  $\beta$  and  $\gamma$  are computed from (4) and (5) using observations of  $w$  and  $\gamma(0)$ . Synoptic maps for the three cases were used to find  $w$ . The temperature observations on the tower, averaged for five minutes, were used to determine  $\frac{\partial \Theta}{\partial t}$  and  $\gamma(0)$ .

The turbulent transport at 45 m was determined by averaging heat

flux measurements from a sonic anemometer-thermometer system that was operated on the tower during October 1971. Complete details of the system are given by Hanafusa (1971). Briefly, the system electronically filters the signals of vertical velocity, temperature and their product. At one minute intervals digital samples are written on magnetic tape. The turbulent flux is found from

$$\overline{(w'\theta')}_{45} = \overline{w\theta} - \overline{w} \overline{\theta}, \quad (15)$$

where the bars indicate a time average of the digital samples. Thirty minutes was the averaging interval used in this study.

Observations of  $h$  were compared to values of  $h$  from this penetrative convection model for all three cases. The results are shown in Fig. 10. This model is successful only for the case without the anomalous temperature fluctuations. The root mean square error, RMSE, is 32.2 m for this case compared to 161 m and 76 m for the other cases. It is thought this shows that some other process is acting toward inversion dissipation on 25 and 28 October. The anomalous temperature fluctuations may be an indicator of breaking waves at inversion base.

The breaking wave parameterization enters the model as an additional term on the right side of (14). The assumption is made that within a time scale  $t^*$ , a breaking wave event takes place. Fig. 9, adapted from Hardy (1972), shows how an event appears as a clear air radar echo.

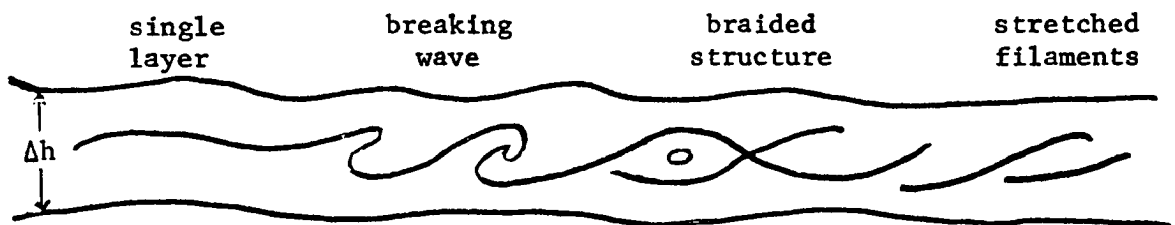


Figure 9. Stages in the development of Kelvin-Helmholtz billow. The dark line corresponds to detectable clear air radar echo.

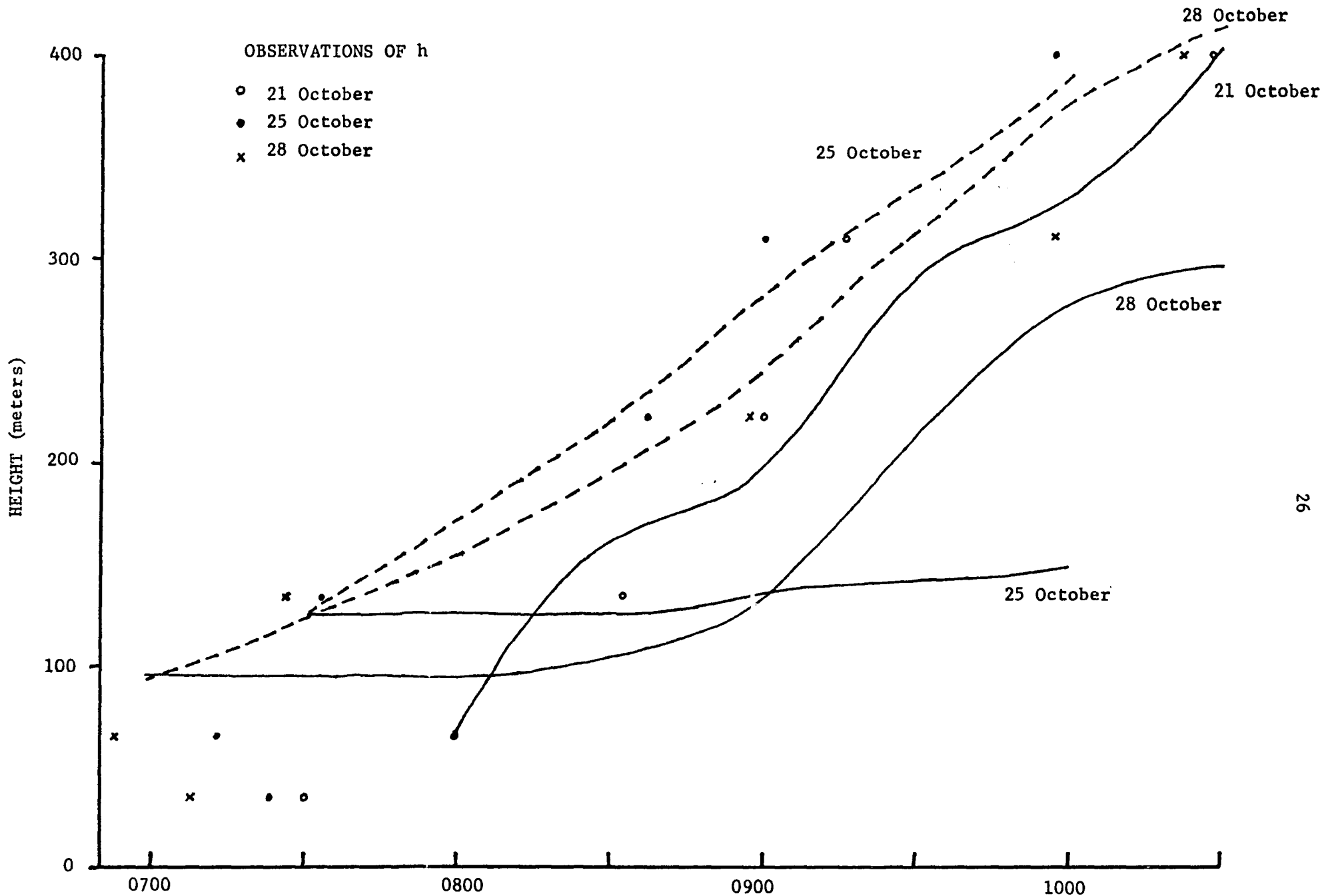


Figure 10. Behavior of inversion base height, h. Observations of h are the points. The penetrative convection model is the solid line. Penetrative convection and breaking wave effects model is the dashed line.

Within the time scale  $t^*$ , the sensible heat per unit area over a depth  $\Delta h$  is assumed to be completely transferred into the mixed layer below the inversion. Eq. (14) is replaced by

$$-\overline{(w'\theta')}_{\text{h}} = C_1 \overline{(w'\theta')}_{\text{o}} + C_2 \frac{\Delta h}{2t^*} (\Delta\theta + \gamma \Delta h). \quad (16)$$

The parameter  $t^*$  is obtained from observations of heat flux at 45 m. Periodic bursts of negative flux in the data are thought to be the result of the culmination of a breaking wave event. The parameter  $\Delta h$  is calculated from the product of the observed rate of rise of the inversion and the duration of the anomalous temperature fluctuations at a given level.

This second model, incorporating breaking wave effects, is (10), (11), (12), (13), and (16). A value of 0.3 for  $C_2$  is used in (16). Fig. 10 shows the result of this model for the two breaking wave cases. The values of  $\Delta h$  are 30 m on 28 October and 70 m on 25 October. The time scale,  $t^*$ , is 522 s on 25 October and 330 s on 28 October. This model is fairly successful in predicting  $h$  for these two cases. The shape of the curves show that the greatest contribution of the breaking waves is in the very early hours when the surface heat flux is small. Table 3 is the errors between the model and observed  $h$  for the different cases. The RMSE on 25 October is reduced from 161 m in the penetrative convection model to 16.8 m in this second model. On 28 October the RMSE is reduced from 76 m to 34 m.

The result of this analysis of the inversion dynamics is to show that there is increased mixing at inversion base over that which

might be expected by penetrative convection alone. Further examination of the data will show that a wind shear type of instability is probably the cause of this increased mixing.

TABLE 3  
ERROR OF MODELS FROM OBSERVED INVERSION BASE HEIGHT

Date	21	25	25	28	28
model	convective	convective	convective + breaking wave	convective	convective + breaking wave
comparison point	error (meters)				
1	0	-8	-2	-39	-19
2	31	-95	13	-94	19
3	-25	-175	-27	-36	62
4	-60	-254	-15	-107	6
5	-2				
Root Mean Square Error	32.2	161.4	16.8	76.0	33.9

## CHAPTER IV

### FURTHER TOWER OBSERVATIONS

The mean wind profiles on 25 and 28 October show strong resemblances to the wind profile of the Ekman wind spiral. These mean profiles are of thirty minute averages of the wind velocity. Hodographs of the wind profile on 25 October are seen in Fig. 11. Along with the actual wind, Ekman spirals are plotted in this figure. These Ekman spirals attempt to match the actual wind profiles. The two profiles agree fairly well except for the wind speed maximum at level 4. The actual wind and the Ekman spiral were required to match exactly at level 5 of the tower for the best fit. From their relationship to the Ekman solution, the geostrophic wind above the boundary layer,  $V_g$ , the characteristic Ekman depth,  $\delta$ , and a Reynolds number,  $Re$ , can all be determined for these mean wind profiles. This information is also found on Fig. 11. The Ekman depth is defined as  $\delta = (2K_m f^{-1})^{\frac{1}{2}}$ , where  $K_m$  is an eddy viscosity and  $f$  is the Coriolis parameter at  $35^{\circ}30'N$ . The Reynolds number is defined as  $Re = V_g \delta / K_m$ . If it is known that the Ekman solutions,

$$u = V_g \left( 1 - \exp \frac{-z}{\delta} \cos \frac{z}{\delta} \right),$$

$$v = V_g \exp \frac{-z}{\delta} \sin \frac{z}{\delta},$$

and the actual wind match at level 5,  $V_g$  and  $\delta$  can be determined. After 0830 CST the wind maximum passed above the tower and it becomes more

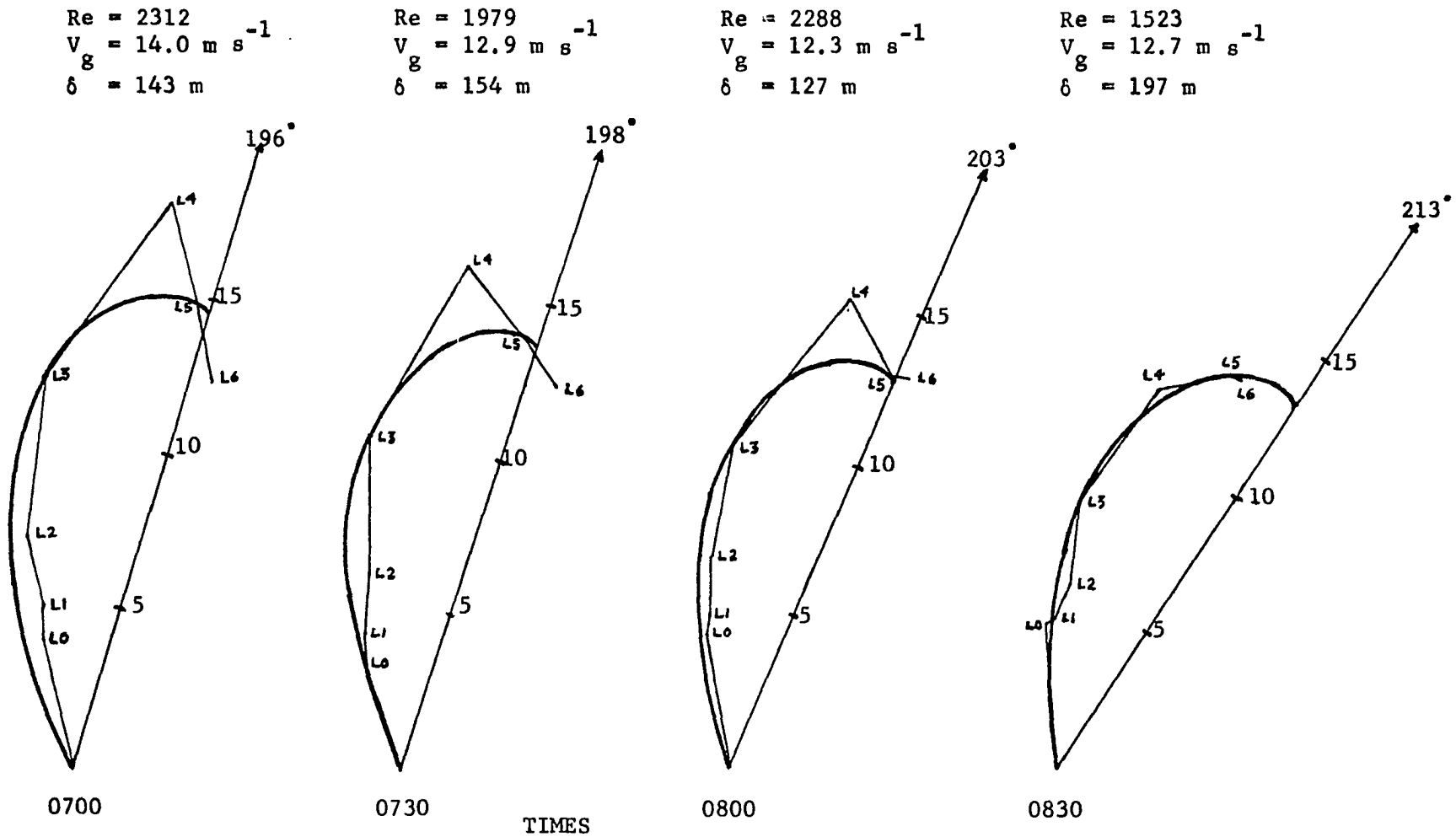


Figure 11. Hodographs of actual wind and Ekman spiral, 25 October 1971. Wind speed is in  $\text{ms}^{-1}$ . Measurement levels are indicated by L0, L1, etc.. The Reynolds number, geostrophic wind speed, and Ekman depth are given above each hodograph. The geostrophic wind direction is the arrow on each hodograph.

difficult to match the actual wind profile with an Ekman spiral.

The theoretical model, which this data is compared to, assumes a two-dimensional structure which is found in the y-z plane. For this reason the wind is decomposed into component wind velocities. Fig. 1 shows the relationship of the component axes to the geostrophic wind. The angle of the longitudinal axis, x, from the direction of  $\underline{V}_g$  is  $\epsilon$ . The parameter  $\epsilon$  will become a variable in the analysis of the data. In Fig. 12 is the 0800 CST lateral velocity components of the actual wind and the Ekman profile in the y-z plane. It is seen there is an inflection point in the component velocity. The inflection point is in the region of significant wind shear below level 4 at 0800 CST.

Further information about these wind profiles is obtained by fitting a cubic polynomial to the wind speeds at tower levels 2 to 5. In this manner the inflection point height was found and the magnitude of the velocity and the vertical shear of the wind at the inflection point estimated. These values are given in Table 4 for different values of  $\epsilon$  at 0700, 0730, 0800, and 0830 CST. Note that the inflection point height is generally moving upward with time.

Mean wind hodographs for 0700, 0730, 0800 and 0830 CST on 28 October are found in Fig. 13. On 28 October the actual wind matches the Ekman profile better than it did on 25 October. The wind speed maximum fits into the spiral very well in this case. An exact match between the two profiles was required at level 4 on this date to give the best fit of the spiral to the actual wind. The parameters  $Re$ ,  $\underline{V}_g$  and  $\delta$  are also listed with the hodographs. How well the Ekman spiral and the actual wind match in a vertical profile are seen for 0730 CST

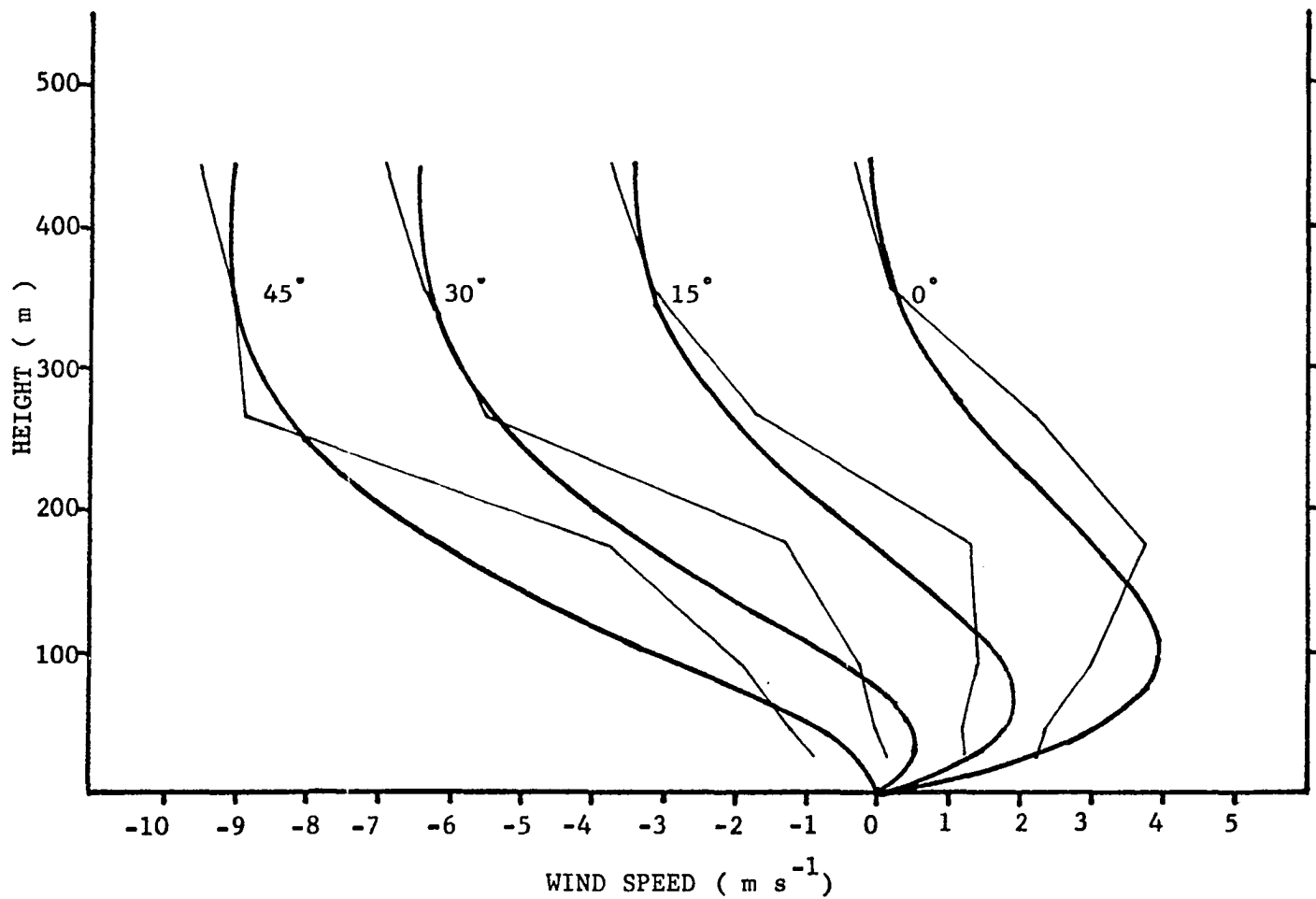


Figure 12. Component wind speed ( $v_y$ ) in the direction of the lateral axis ( $y$ ) for different values of  $\epsilon$ . The thin line is the component of the actual wind and the heavy line is the component of the Ekman spiral. The time is 0800 CST on 25 October 1971.

TABLE 4

PARAMETERS OF THE BOUNDARY LAYER FOR 25 OCTOBER 1971

Time	$\epsilon$	$z_{ip}$ (m)	$v_{ip}$ (m s <sup>-1</sup> )	$\frac{\partial v}{\partial z}_{ip}$ (s <sup>-1</sup> )	$Ri_1$	$Ri_b$	$\lambda$ (m)	$\alpha^*$ (1/8)	$\alpha^* c_i$ (s <sup>-1</sup> )
0700	20°	220	-1.91	-0.0491	0.2718	0.0234			
	25°	215	-2.95	-0.0543	0.2223	0.0230			
	30°	212	-4.03	-0.0591	0.1876	0.0231			
	35°	209	-5.06	-0.0637	0.1615	0.0235			
	40°	206	-6.02	-0.0678	0.1426	0.0249			
	45°	204	-6.98	-0.0716	0.1278	0.0266			
	50°	202	-7.88	-0.0748	0.1171	0.0290			
	60°	200	-8.67	-0.0776	0.1088	0.0320			
0730	20°	235	-1.51	-0.0391	0.2378	0.0206			
	25°	228	-2.43	-0.0438	0.1895	0.0196			
	30°	223	-3.35	-0.0484	0.1552	0.0191			
	35°	220	-4.32	-0.0529	0.1299	0.0190			
	40°	215	-5.11	-0.0571	0.1115	0.0195			
	45°	213	-6.01	-0.0609	0.0980	0.0204			
	50°	210	-6.78	-0.0644	0.0877	0.0217			
	60°	208	-7.54	-0.0675	0.0798	0.0232			
0800	20°	229	-1.57	-0.0413	0.1491	0.0129	673	1.186	<0.0
	25°	224	-2.47	-0.0460	0.1202	0.0124	1059	0.753	0.00256
	30°	220	-3.36	-0.0505	0.0997	0.0123	1440	0.554	0.01219
	35°	217	-4.27	-0.0546	0.0853	0.0125	1830	0.436	0.01305
	40°	215	-5.12	-0.0585	0.0743	0.0130	2194	0.364	0.01125
	45°	212	-5.88	-0.0619	0.0664	0.0138	2520	0.317	0.00882
	50°	210	-6.65	-0.0650	0.0602	0.0149	2850	0.280	0.00616
	60°	208	-7.35	-0.0676	0.0557	0.0164	3150	0.253	0.00348
0830	20°	304	-1.22	-0.0238	0.1971	0.0171			
	25°	280	-1.74	-0.0257	0.1691	0.0175			
	30°	267	-2.46	-0.0282	0.1404	0.0173			
	35°	255	-3.11	-0.0309	0.1169	0.0171			
	40°	250	-3.91	-0.0336	0.0989	0.0173			
	45°	240	-4.48	-0.0362	0.0852	0.0177			
	50°	235	-5.15	-0.0387	0.0746	0.0185			
	60°	233	-5.89	-0.0409	0.0667	0.0197			
		230	-6.53	-0.0430	0.0604	0.0212			

$Re = 3149$   
 $V_g = 14.4 \text{ m s}^{-1}$   
 $\delta = 108 \text{ m}$

$Re = 2233$   
 $V_g = 13.9 \text{ m s}^{-1}$   
 $\delta = 147 \text{ m}$

$Re = 1715$   
 $V_g = 14.3 \text{ m s}^{-1}$   
 $\delta = 197 \text{ m}$

$Re = 1650$   
 $V_g = 13.9 \text{ m s}^{-1}$   
 $\delta = 199 \text{ m}$

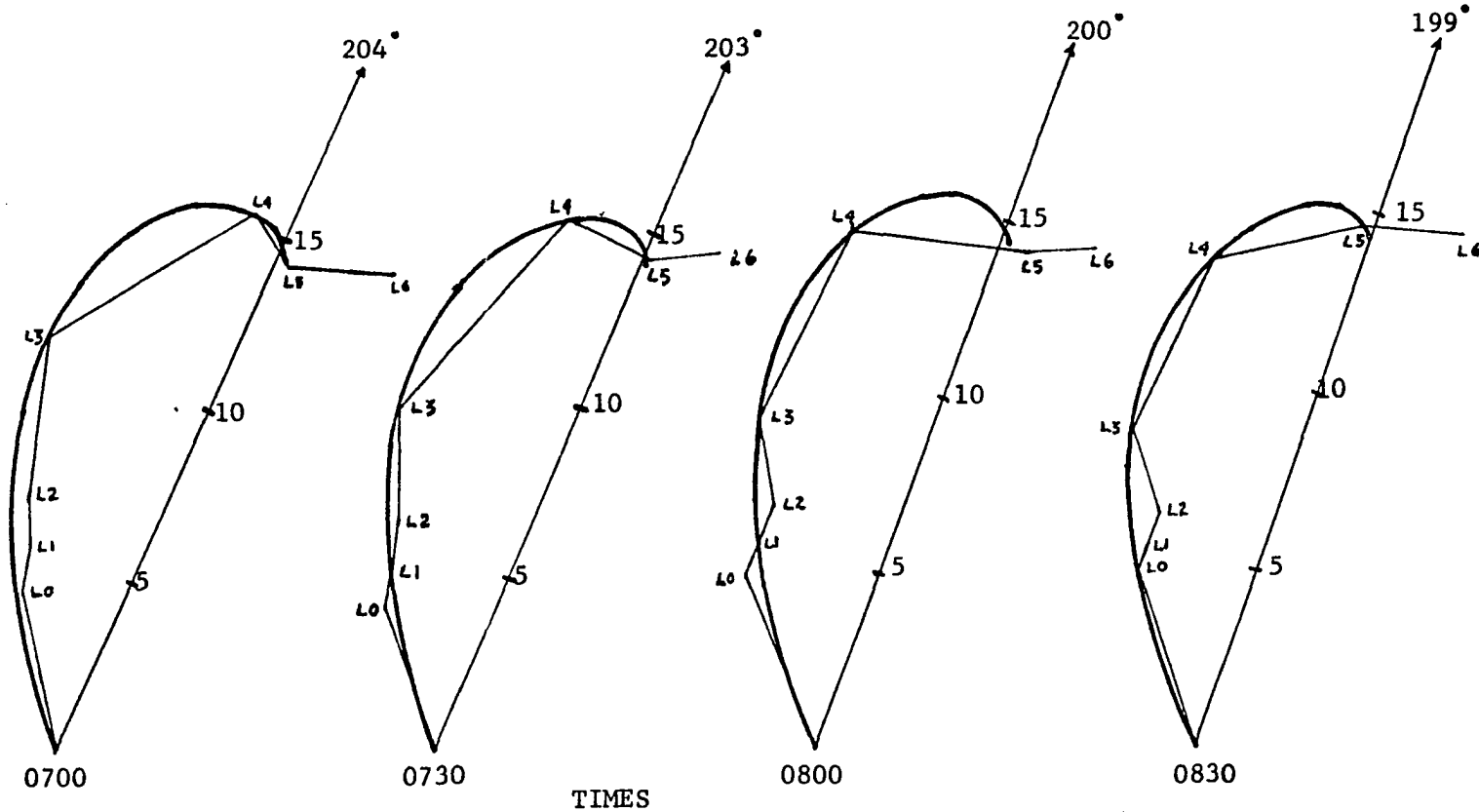


Figure 13. Hodographs of actual wind and Ekman spiral, 28 October 1971. Wind speed in  $\text{m s}^{-1}$ . Measurement levels are indicated by L0, L1, etc.. The Reynolds number, geostrophic wind speed, and Ekman depth are given above each hodograph. The geostrophic wind direction is the arrow on each hodograph.

in Fig. 14. This figure shows the lateral component velocity at the different heights for several different values of  $\epsilon$ .

A further analysis of the mean wind is the fit of a cubic polynomial to the wind speed at levels 2 to 5 of the tower. Table 5 lists the height of the inflection point in the wind speed and the velocity and the vertical shear of the wind at this inflection point. As on 25 October the inflection point occurs near inversion base which is below the location of the temperature fluctuations. Again with time the height of the inflection point rises.

The stability parameter for the boundary layer is chosen to be the Richardson number. A local Richardson number,  $Ri_1$ , is defined as

$$Ri_1 = \frac{g \frac{\partial \theta}{\partial z}}{\bar{\theta} \left| \frac{\partial v}{\partial z} \right|_{ip}^2}$$

Values of potential temperature gradient  $\partial\theta/\partial z$  and average potential temperature,  $\bar{\theta}$ , were estimated from the tower data. The estimates are for the layer between the tower levels immediately beneath the inflection point. Table 6 shows these estimates. The values are eleven minute averages centered at the times given.

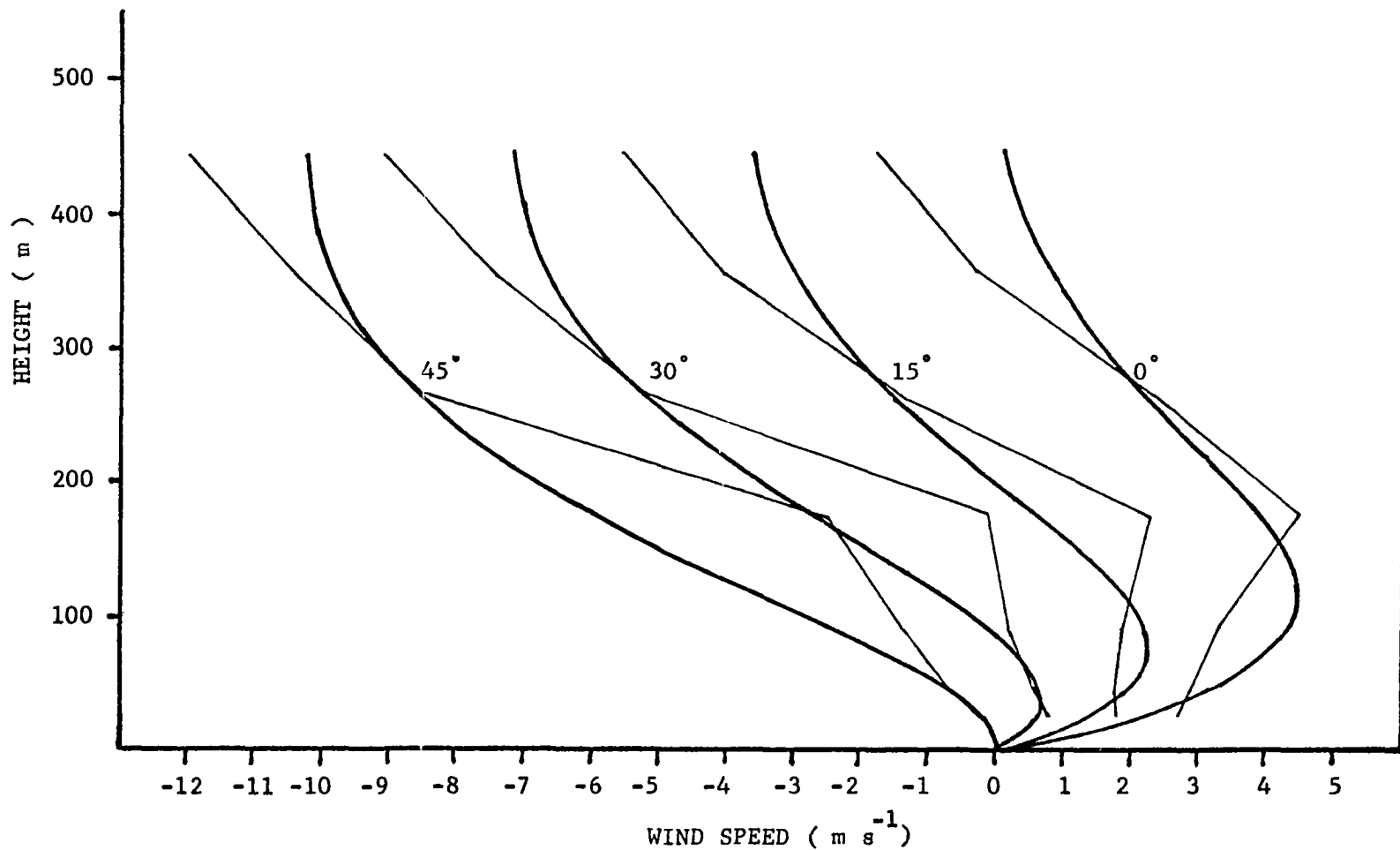


Figure 14. Component wind speed ( $v$ ) in the direction of the lateral axis ( $y$ ) for different values of  $\epsilon$ . The thin line is the component of the actual wind and the heavy line is the component of the Ekman spiral. The time is 0730 CST on 28 October 1971.

TABLE 5

PARAMETERS OF THE BOUNDARY LAYER FOR 28 OCTOBER 1971

Time	$\epsilon$	$Z_{ip}$ (m)	$V_{ip}$ ( $m s^{-1}$ )	$\frac{\partial v}{\partial z}_{ip}$ ( $s^{-1}$ )	$Ri_l$	$Ri_b$	$\lambda$ (m)	$\alpha^*$ ( $1/\delta$ )	$\alpha^* c_i$ ( $s^{-1}$ )
0700	20°	225	-1.86	-0.0636	0.1240	0.0108			
	25°	222	-2.82	-0.0669	0.1121	0.0116			
	30°	220	-3.83	-0.0698	0.1029	0.0127			
	35°	218	-4.80	-0.0722	0.0962	0.0141			
	40°	216	-5.70	-0.0741	0.0914	0.0159			
	45°	214	-6.50	-0.0755	0.0880	0.0183			
	50°	212	-7.40	-0.0765	0.0857	0.0212			
	55°	210	-8.13	-0.0769	0.0848	0.0250			
	60°	207	-8.72	-0.0768	0.0850	0.0298			
0730	20°	240	-1.47	-0.0513	0.1027	0.0089	588	1.570	<0.0
	25°	237	-2.44	-0.0560	0.0862	0.0089	976	0.946	<0.0
	30°	233	-3.30	-0.0605	0.0739	0.0091	1320	0.700	0.00645
	35°	230	-4.17	-0.0646	0.0648	0.0095	1668	0.554	0.01194
	40°	227	-4.98	-0.0683	0.0580	0.0101	1992	0.464	0.01192
	45°	225	-5.80	-0.0716	0.0527	0.0109	2320	0.398	0.01044
	50°	223	-6.57	-0.0743	0.0490	0.0121	2628	0.351	0.00833
	55°	221	-7.28	-0.0766	0.0461	0.0136	2912	0.317	0.00597
	60°	220	-8.00	-0.0784	0.0440	0.0154	3200	0.289	0.00343
0800	20°								
	25°	355	-6.85	-0.0537	0.0543	0.0056			
	30°	305	-5.46	-0.0506	0.0612	0.0075			
	35°	280	-5.40	-0.0511	0.0600	0.0088			
	40°	265	-5.76	-0.0529	0.0560	0.0098			
	45°	255	-6.30	-0.0551	0.0516	0.0107			
	50°	247	-6.85	-0.0574	0.0476	0.0118			
	55°	240	-7.38	-0.0596	0.0441	0.0130			
	60°	235	-7.94	-0.0617	0.0412	0.0144			
0830	20°	376	-5.80	-0.0489	0.0511	0.0044			
	25°	322	-5.48	-0.0455	0.0590	0.0061			
	30°	295	-4.49	-0.0459	0.0579	0.0071			
	35°	275	-4.74	-0.0477	0.0537	0.0079			
	40°	265	-5.37	-0.0501	0.0486	0.0085			
	45°	255	-5.90	-0.0526	0.0441	0.0092			
	50°	250	-6.61	-0.0551	0.0402	0.0099			
	55°	245	-7.25	-0.0574	0.0371	0.0109			
	60°	240	-7.81	-0.0595	0.0345	0.0121			

TABLE 6  
VERTICAL GRADIENT OF POTENTIAL TEMPERATURE AND MEAN POTENTIAL  
TEMPERATURE FOR THE LAYER

Date	Time	Layer	$\frac{\partial \theta}{\partial z}$ (K/m)	$\bar{\theta}$ (K)
25 October 1971	0700	90-176 m	0.0193	288.6
	0730	90-176 m	0.0107	288.4
	0800	90-176 m	0.0075	288.9
	0830	90-176 m	0.0033	288.6
28 October 1971	0700	90-176 m	0.0148	288.5
	0730	90-176 m	0.0080	288.5
	0800	90-176 m	0.0046	288.3
	0830	90-176 m	0.0036	288.9

The shear term,  $|\partial v / \partial z|_{ip}$ , is the value of the vertical shear of the wind at the inflection point and is obtained from fitting the cubic polynomial to the wind. The shear values are found in Table 4. Also in Table 4 are values of  $Ri_1$  for several values of  $\epsilon$ . A bulk Richardson number,  $Ri_b$ , which the theoretical model requires, is obtained by dividing the shear,  $|\partial v / \partial z|_{ip}$ , which is dimensional, by the non-dimensional shear of the Ekman wind profile at its inflection point and substituting this bulk shear for  $|\partial v / \partial z|_{ip}$ . The bulk shear is

$$\left| \frac{\partial v}{\partial z} \right|_b = \frac{\left| \frac{\partial v}{\partial z} \right|_{ip} \text{ (observed)}}{\left| \frac{\partial v}{\partial z} \right|_{ip} \text{ (Ekman wind)}} = \frac{V}{\delta},$$

where  $\left| \frac{\partial v}{\partial z} \right|_{ip} = -\exp(\pi/2 - \epsilon)$  for the Ekman wind. This procedure expresses the shear in terms of the scaling parameters. Thus the  $Ri_b$  shear term is the ratio of the velocity scale to the height scale of the model. Table 4 lists the local and bulk Richardson numbers for the

different  $\epsilon$  and times.

The exact structure of the instability causing the temperature fluctuations is impossible to determine from a single tower. A reasonable estimate of the horizontal wavelength of the instability is possible, however. This estimate relies on measurements of the frequency and phase speed of the instability as measured on the tower. The frequency is derived from the anomalous temperature fluctuations. The inflection point instability model assumes the same harmonic form for both the wind and temperature perturbations. Therefore the visual and power spectrum analysis of the level 4 temperature fluctuations supply a frequency of  $0.14 \text{ cycles min}^{-1}$  on 25 October for the lowest frequency mode of the instability. Also consistent with the theoretical instability model, the phase speed is the lateral wind velocity component at the inflection point. This is listed for different values of  $\epsilon$  in Table 4. It is necessary to have estimates of wavelength for many values of  $\epsilon$  because the exact orientation of the instability is unknown. Later the best match between observations and model will indicate the probable orientation of the instability. The wavelength,  $\lambda$ , is found from  $\lambda = c_r/q$ , where  $c_r$  is the real phase velocity and  $q$  is the frequency. On 25 October, 0800 CST is the most representative time for the estimate of frequency. Therefore estimates of wavelength for different  $\epsilon$  are tabulated in Table 4 only for 0800 CST on 25 October.

The stability of the boundary layer on 28 October is given by the local and bulk Richardson numbers in Table 5. The potential temperature gradient estimates are from the layer below the inflection points shown in Table 5. Table 6 has the mean potential temperature and vertical

gradient of potential temperature for these layers.

The structure of the instability as indicated by the horizontal wavelength is given for 0730 CST in Table 5. The estimate of frequency,  $0.15 \text{ cycles min}^{-1}$ , is from the visual and power spectrum analysis of the temperature fluctuations at level 4. It is most representative at 0730 CST.

As has been indicated the mean profiles and fluctuating quantities in the boundary layer are very similar for 25 and 28 October. The actual wind structures are very close to that of the Ekman spiral wind profile. Significant features are the low-level wind maximum and an inflection point in the vertical profile of wind speed. The wind speed maximum is found near inversion top and moves upward with the inversion. The inflection point however, is located near inversion base where strong vertical wind shear causes low Richardson numbers in this region. Some type of instability is indicated by anomalous temperature fluctuations occurring in a shallow layer above inversion base. The instability continues as the inversion rises through the tower layer. The next section discusses the various types of instabilities associated with the Ekman boundary layer to see if one of them might be responsible for these temperature fluctuations.

## CHAPTER V

### THE EKMAN LAYER INSTABILITIES

The source of the temperature fluctuations is sought in the instabilities of the Ekman boundary layer. There are four known instability mechanisms associated with the Ekman layer. They are convective instability, parallel instability, resonance with internal waves, and inflection point instability. At the locus of its maximum growth rate each instability mode has its own preferred wavelength and orientation from the geostrophic wind. This orientation angle is called  $\epsilon$  and is the angle of the longitudinal axis,  $x$ , from the geostrophic wind (see Fig. 1)

The convective instability is a thermal instability occurring in unstable stratification. It operates by conversion of potential to kinetic energy through upward heat transport. Asai and Nakasuji (1973) found this mode is preferred for a bulk Richardson number less than  $-10^{-3}$ . They cite for it a horizontal wavelength of  $2\pi\delta$ , a phase velocity equal to  $V_g$  and they find it has no preferred orientation angle.

The parallel instability is discussed by Lilly (1966). It is a shear instability drawing energy from the mean flow along the longitudinal axis of the disturbance and supplying it to the lateral component via the Coriolis force. The parallel instability becomes insignificant for Reynolds numbers greater than 150. This mode has a preferred wavelength of  $6.7\pi\delta$ , an orientation angle,  $\epsilon$ , of  $10^\circ$  to the right of  $\underline{V}_g$ ,

and a phase velocity near that of the mean flow at the inflection point height in the direction of the lateral axis of the instability.

For low values of positive Richardson number, those between 0 and 0.25, the growth rates of instability in the Ekman layer decrease with increasing Richardson number. Kaylor and Faller (1972) have found an instability occurring at significantly larger  $Ri$  due to the resonance of the incipient instability with internal gravity waves. This instability develops in the region of large wind shear and feeds into a gravitational wave which occupies the upper stable region. The phase speed is some velocity that is possible for both the internal wave and the shear instability. The wavelength and orientation have not been clearly defined for this instability. It appears the Coriolis force is an essential energy transfer mechanism in this instability.

Lilly (1966) also demonstrated the inflection point instability for an Ekman velocity profile. Inflection point instability is an inviscid instability that has been widely studied in plane flow with an inflection point in the mean velocity profile. The inflection point represents a vorticity extremum in the mean vorticity profile. Brown (1972b) describes the onset of this instability as a result of the fluid's inability to support this extremum. It should be remembered we are speaking of the component of vorticity perpendicular to the  $y$ - $z$  plane. In a monotonically increasing or decreasing vorticity profile an infinitesimally displaced parcel distorts the vorticity profile. Lin (1945) has derived the formula for a restoring force this distorted vortex field exerts on the displaced parcel. Thus the parcel is returned to its origin and there is no instability. In a vorticity profile with

an extremum, a parcel displaced across the velocity inflection point will experience a force such that it is moved to a position compatible with its original vorticity but on the opposite side of the extremum. If the displaced vortex carries its original momentum with it, this nonlinear mean momentum transport will distort the mean velocity profile such that there now appear two inflection points. Thus further growth of the instability is encouraged. The inflection point instability is the preferred mode for Reynolds numbers greater than 150 and a bulk Richardson number between  $-10^{-3}$  and  $\frac{1}{2}$ . For a neutral atmosphere it has a preferred wavelength of  $4\pi\delta$ , the orientation  $\epsilon$  is  $20^\circ$  to the left of  $\vec{V}_g$  and the phase velocity is near the mean velocity at inflection point height in the direction of the lateral axis of the instability.

Brown has developed an inflection point instability model of the Ekman layer for both the neutral (Brown, 1970) and the stratified (Brown, 1972a) Ekman boundary layer. Brown's (1972a) model develops unstable infinitesimal perturbations in the form of counter-rotating roll vortices. The most unstable growth rates occur with the instability longitudinal axis oriented  $20^\circ$  to the left of  $\vec{V}_g$ , the lateral wavelength is  $4\pi\delta$ , and the vertical dimension is 5 to 7  $\delta$ . This is for neutral stratification. Unstable stratification shows greater amplification, with the convective instability becoming dominant for increasingly negative Ri. Damping of the instability is found for a stable stratification. The instability mode is completely extinguished for a local Richardson number exceeding 0.25. At values of Ri close to this, the region of instability becomes limited to wavelengths close to

$4\pi\delta$  and an orientation angle of  $35^\circ$ .

The choice of which possible instability mechanism to consider as the source of the temperature fluctuations is made by examining the data. The convective type seems unlikely because of the positive  $Ri$ . Also there is no resemblance between the afternoon temperature fluctuations which are caused by convection and the morning temperature fluctuations observed at a single level. The previous analysis of penetrative convection further indicates the lesser importance of this instability. The parallel instability mode is rejected mainly on the basis of the large observed Reynolds numbers. The resonance instability mode would have the development of the instability throughout the stable layer. Because these temperature fluctuations appear to be confined to the lower less stable regions of the inversion, this instability was not considered to be a possible source. It is in the inflection point instability mode that the greatest agreement occurs between the data and the model. The large Reynolds number, estimated wavelengths near  $4\pi\delta$ , and the presence of the large wind shear at an inflection point coinciding with the region of temperature fluctuations encourages further investigation of this instability mode.

## CHAPTER VI

### THE INFLECTION POINT INSTABILITY MODEL

The inflection point instability mechanism will be investigated with a linear infinitesimal perturbation model. The perturbations are assumed harmonic functions and will be considered to be unstable if they increase in amplitude with time.

The initial assumptions in deriving the equations to describe this boundary layer phenomenon are to neglect the viscous terms and write the Reynolds stress terms in the form of an eddy viscosity with constant coefficient. The equations of motion are written in a Cartesian coordinate system. The continuity equation is expressed in the incompressible form by making the Boussinesq approximation of neglecting density variations except in the buoyancy term of the vertical momentum equation. According to Spiegel and Veronis (1960), this is possible when the vertical dimension of the fluid is much less than the scale height of the fluid. In this study the boundary layer thickness is much less than the scale height of an atmosphere which is assumed adiabatic. The thermodynamic equation has the addition of a diffusion term to account for eddy transport of heat in the boundary layer. The dimensional set of equations is then

$$\frac{\partial u^*}{\partial t} + u^* \frac{\partial u^*}{\partial x} + v^* \frac{\partial u^*}{\partial y} + w^* \frac{\partial u^*}{\partial z} - fv^* + \frac{1}{\rho_m^*} \frac{\partial p^*}{\partial x} - K_m \left( \frac{\partial^2 u^*}{\partial x^2} + \frac{\partial^2 u^*}{\partial y^2} + \frac{\partial^2 u^*}{\partial z^2} \right) = 0 ,$$

$$\frac{\partial v^*}{\partial t} + u^* \frac{\partial v^*}{\partial x} + v^* \frac{\partial v^*}{\partial y} + w^* \frac{\partial v^*}{\partial z} + fu^* + \frac{1}{\rho_m^*} \frac{\partial p^*}{\partial y} - K_m \left( \frac{\partial^2 v^*}{\partial x^2} + \frac{\partial^2 v^*}{\partial y^2} + \frac{\partial^2 v^*}{\partial z^2} \right) = 0 ,$$

$$\frac{\partial w^*}{\partial t} + u^* \frac{\partial w^*}{\partial x} + v^* \frac{\partial w^*}{\partial y} + w^* \frac{\partial w^*}{\partial z} + g + \frac{1}{\rho_m^*} \frac{\partial p^*}{\partial z} - K_m \left( \frac{\partial^2 w^*}{\partial x^2} + \frac{\partial^2 w^*}{\partial y^2} + \frac{\partial^2 w^*}{\partial z^2} \right) = 0 ,$$

$$\frac{\partial u^*}{\partial x} + \frac{\partial v^*}{\partial y} + \frac{\partial w^*}{\partial z} = 0 ,$$

(17)

$$p^* = \rho^* R T^* ,$$

$$\frac{\partial T^*}{\partial t} + u^* \frac{\partial T^*}{\partial x} + v^* \frac{\partial T^*}{\partial y} + w^* \frac{\partial T^*}{\partial z} + w^* \frac{g}{C_p} - K_h \left( \frac{\partial^2 T^*}{\partial x^2} + \frac{\partial^2 T^*}{\partial y^2} + \frac{\partial^2 T^*}{\partial z^2} \right) = 0 ,$$

where the definitions of the symbols are given in Table 1. The stars indicate the variables are dimensional. The coordinates are unstarred for convenience. These equations are now made non-dimensional with the following parameters:

$$u^* = V_g u, \quad v^* = V_g v, \quad w^* = V_g \frac{H}{L} w, \quad x = Lx, \quad y = Ly,$$

$$z = Hz, \quad p^* = Pp, \quad \rho^* = \bar{\rho} \rho, \quad \rho_m^* = \bar{\rho} \rho_m, \quad (18)$$

$$T^* = \bar{\Theta} T, \quad t = \frac{L}{V_g} t.$$

The space and time coordinates are dimensional when written with dimensional variables and are non-dimensional otherwise. Eqs. (17) now are written,

$$\frac{V_g^2}{L} \left( \frac{\partial u}{\partial t} + u \frac{\partial u}{\partial x} + v \frac{\partial u}{\partial y} + w \frac{\partial u}{\partial z} \right) - f V_g v + \frac{P}{\rho_L} \frac{1}{\rho_m} \frac{\partial p}{\partial x} - \frac{K V_g}{L^2} \left( \frac{\partial^2 u}{\partial x^2} + \frac{\partial^2 u}{\partial y^2} \right) - \frac{K V_g}{H^2} \frac{\partial^2 u}{\partial z^2} = 0,$$

$$\frac{V_g^2}{L} \left( \frac{\partial v}{\partial t} + u \frac{\partial v}{\partial x} + v \frac{\partial v}{\partial y} + w \frac{\partial v}{\partial z} \right) + f V_g u + \frac{P}{\rho_L} \frac{1}{\rho_m} \frac{\partial p}{\partial y} - \frac{K V_g}{L^2} \left( \frac{\partial^2 v}{\partial x^2} + \frac{\partial^2 v}{\partial y^2} \right) - \frac{K V_g}{H^2} \frac{\partial^2 v}{\partial z^2} = 0, \quad (19)$$

$$\frac{H V_g^2}{L^2} \left( \frac{\partial w}{\partial t} + u \frac{\partial w}{\partial x} + v \frac{\partial w}{\partial y} + w \frac{\partial w}{\partial z} \right) + g + \frac{P}{\rho_H} \frac{1}{\rho} \frac{\partial p}{\partial z} - \frac{K V_g H}{L^3} \left( \frac{\partial^2 w}{\partial x^2} + \frac{\partial^2 w}{\partial y^2} \right) - \frac{K V_g}{L H} \frac{\partial^2 w}{\partial z^2} = 0,$$

$$\frac{\partial u}{\partial x} + \frac{\partial v}{\partial y} + \frac{\partial w}{\partial z} = 0, \quad p = \frac{\bar{\rho} \bar{\Theta} R}{P} \rho T,$$

$$\frac{V_g \bar{\Theta}}{L} \left( \frac{\partial T}{\partial t} + u \frac{\partial T}{\partial x} + v \frac{\partial T}{\partial y} + w \frac{\partial T}{\partial z} \right) + \frac{V_g H}{L} w \frac{g}{C_p}$$

$$- \frac{K_h \bar{\Theta}}{L^2} \left( \frac{\partial^2 T}{\partial x^2} + \frac{\partial^2 T}{\partial y^2} \right) - \frac{K_h \bar{\Theta}}{H^2} \frac{\partial^2 T}{\partial z^2} = 0.$$

The following non-dimensional parameters will be used:

$$Re = \frac{V_g H}{K_m} \quad \text{a Reynolds number,}$$

$$Ro = \frac{V_g}{fL} \quad \text{a Rossby number,}$$

$$\begin{aligned} \Pi &= \frac{P}{V_g^2}, \quad \text{Pr} = \frac{K_m}{K_h} \quad \text{a Prandtl number,} \\ g_o &= \frac{gH}{V_g^2}, \quad \chi = \frac{H}{L} \quad \text{an aspect ratio.} \end{aligned} \tag{20}$$

With these, (19) is written as

$$\begin{aligned} \text{Ro} \left( \frac{\partial u}{\partial t} + u \frac{\partial u}{\partial x} + v \frac{\partial u}{\partial y} + w \frac{\partial u}{\partial z} \right) - v + \frac{\text{Ro}\Pi}{\rho_m} \frac{\partial P}{\partial x} \\ - \frac{\text{Ro}\chi}{\text{Re}} \left( \frac{\partial^2 u}{\partial x^2} + \frac{\partial^2 u}{\partial y^2} \right) - \frac{K_m}{fH^2} \frac{\partial^2 u}{\partial z^2} = 0, \\ \text{Ro} \left( \frac{\partial v}{\partial t} + u \frac{\partial v}{\partial x} + v \frac{\partial v}{\partial y} + w \frac{\partial v}{\partial z} \right) + u + \frac{\text{Ro}\Pi}{\rho_m} \frac{\partial P}{\partial y} \\ - \frac{\text{Ro}\chi}{\text{Re}} \left( \frac{\partial^2 v}{\partial x^2} + \frac{\partial^2 v}{\partial y^2} \right) - \frac{K_m}{fH^2} \frac{\partial^2 v}{\partial z^2} = 0, \\ \chi^2 \left( \frac{\partial w}{\partial t} + u \frac{\partial w}{\partial x} + v \frac{\partial w}{\partial y} + w \frac{\partial w}{\partial z} \right) + g_o + \frac{\Pi}{\rho} \frac{\partial P}{\partial z} \\ - \frac{\chi^3}{\text{Re}} \left( \frac{\partial^2 w}{\partial x^2} + \frac{\partial^2 w}{\partial y^2} \right) - \frac{\chi}{\text{Re}} \frac{\partial^2 w}{\partial z^2} = 0, \end{aligned} \tag{21}$$

$$\frac{\partial u}{\partial x} + \frac{\partial v}{\partial y} + \frac{\partial w}{\partial z} = 0, \quad p = \frac{\bar{\rho} \bar{\Theta} R}{p} \rho T,$$

$$\begin{aligned} \text{Ro} \left( \frac{\partial T}{\partial t} + u \frac{\partial T}{\partial x} + v \frac{\partial T}{\partial y} + w \frac{\partial T}{\partial z} \right) + \frac{\text{Ro}H}{\bar{\Theta}} w \frac{g}{C_p} \\ - \frac{\text{Ro}\chi}{\text{RePr}} \left( \frac{\partial^2 T}{\partial x^2} + \frac{\partial^2 T}{\partial y^2} \right) - \frac{K_m}{fH^2 \text{Pr}} \frac{\partial^2 T}{\partial z^2} = 0. \end{aligned}$$

A scale analysis is made of these equations using a small parameter expansion of the variables. This is done by writing the variables

as power series in some small parameter. The series are then substituted for the variables in (21). For each of the powers of the small parameter, the coefficients of the parameter constitute a separate set of equations. The scale of motion governed by each set is dependent upon how much less than one the small parameter is. Thus, it is possible to obtain a set of equations for the mean flow, a second set for the secondary flow and so on. In many cases it is possible to separate a nonlinear set of equations into several sets of linear equations. The final solution to the problem is obtained by summing the original power series.

For this study the interest is on the first order perturbation to the mean flow. The small parameter chosen is  $\chi$ . Many boundary layer phenomena are limited in their vertical extent but have no such limit in the horizontal dimensions. The particular cases of this study have an inversion which limits the vertical dimension to the order of  $\delta$ . For this reason it is expected the aspect ratio,  $\chi = H/L$ , is less than one. The power series expansions of the variables are

$$\begin{aligned}
 u &= u'_0 + \chi u'_1 + \chi^2 u'_2 + \dots, \\
 v &= v'_0 + \chi v'_1 + \chi^2 v'_2 + \dots, \\
 w &= w'_0 + \chi w'_1 + \chi^2 w'_2 + \dots, \\
 p &= p'_0 + \chi p'_1 + \chi^2 p'_2 + \dots, \\
 \rho &= \rho'_0 + \chi \rho'_1 + \chi^2 \rho'_2 + \dots, \\
 T &= T'_0 + \chi T'_1 + \chi^2 T'_2 + \dots.
 \end{aligned}
 \tag{22}$$

Consistent with the Boussinesq approximation,  $\rho_m$  will be equal to  $\rho'_0$  in the horizontal momentum equations. The variables,  $u'_0$ ,  $v'_0$ , etc. are of the order one, but  $\chi < 1$  for the convergence of the power series.

Inserting (22) into (21) and collecting terms of zero order in  $\chi$ , one obtains a set of equations

$$\text{Ro} \left( \frac{\partial u'_0}{\partial t} + u'_0 \frac{\partial u'_0}{\partial x} + v'_0 \frac{\partial u'_0}{\partial y} + w'_0 \frac{\partial u'_0}{\partial z} \right) - v'_0 + \frac{\text{Ro} \Pi}{\rho'_0} \frac{\partial p'_0}{\partial x} - \frac{K_m}{fH^2} \frac{\partial^2 u'_0}{\partial z^2} = 0,$$

$$\text{Ro} \left( \frac{\partial v'_0}{\partial t} + u'_0 \frac{\partial v'_0}{\partial x} + v'_0 \frac{\partial v'_0}{\partial y} + w'_0 \frac{\partial v'_0}{\partial z} \right) + u'_0 + \frac{\text{Ro} \Pi}{\rho'_0} \frac{\partial p'_0}{\partial y} - \frac{K_m}{fH^2} \frac{\partial^2 v'_0}{\partial z^2} = 0,$$

$$g_0 + \frac{\Pi}{\rho'_0} \frac{\partial p'_0}{\partial z} = 0,$$

(23)

$$\frac{\partial u'_0}{\partial x} + \frac{\partial v'_0}{\partial y} + \frac{\partial w'_0}{\partial z} = 0,$$

$$p'_0 = \frac{\bar{\rho} \bar{\Theta} R}{p} \rho'_0 T'_0,$$

$$\text{Ro} \left( \frac{\partial T'_0}{\partial t} + u'_0 \frac{\partial T'_0}{\partial x} + v'_0 \frac{\partial T'_0}{\partial y} + w'_0 \frac{\partial T'_0}{\partial z} \right) + \frac{\text{Ro} H}{\bar{\Theta}} w'_0 \frac{g}{C_p}$$

$$- \frac{K_h}{fH^2 \text{Pr}} \frac{\partial^2 T'_0}{\partial z^2} = 0.$$

This set represents those atmospheric conditions not influenced by the magnitude of  $\chi$  and the solution to (23) is the mean flow. Further simplification of these equations is possible if we assume horizontal uniformity of  $u'_0$ ,  $v'_0$ ,  $T'_0$  and that  $w'_0 = 0$ . The zero-order equations with these simplifications are

$$\begin{aligned}
-v'_0 + \frac{Ro\Pi}{\rho'_0} \frac{\partial p'_0}{\partial x} - \frac{K_m}{fH^2} \frac{\partial^2 u'_0}{\partial z^2} &= 0, \\
u'_0 + \frac{Ro\Pi}{\rho'_0} \frac{\partial p'_0}{\partial y} - \frac{K_m}{fH^2} \frac{\partial^2 v'_0}{\partial z^2} &= 0, \\
g_0 + \frac{\Pi}{\rho'_0} \frac{\partial p'_0}{\partial z} &= 0,
\end{aligned} \tag{24}$$

$$p'_0 = \frac{\bar{p} - \bar{\theta} R}{P} \rho'_0 T'_0, \quad \frac{\partial^2 T'_0}{\partial z^2} = 0.$$

The thermodynamic equation implies  $\frac{\partial T'_0}{\partial z} = \text{constant}$ . The solution to the momentum equations is the Ekman spiral solution

$$\begin{aligned}
u'_0 &= 1 - e^{-z} \cos z, \\
v'_0 &= e^{-z} \sin z,
\end{aligned} \tag{25}$$

with boundary conditions at  $z = 0$  of  $u'_0 = v'_0 = 0$ , and as  $z \rightarrow \infty$ ,  $v'_0 = 0$ ,  $u'_0 = v_g$ . Also

$$v_g = -\frac{P}{f\rho L} \frac{1}{\rho'_0} \frac{\partial p'_0}{\partial y}, \quad H = \delta = \left(\frac{2K_m}{f}\right)^{\frac{1}{2}}, \tag{26}$$

and  $u'_0$  is taken to be in the same direction as  $\underline{v}_g$ .

The set of first-order equations from (21), (22) and using the assumptions on  $u'_0$ ,  $v'_0$ ,  $w'_0$  and  $T'_0$  is

$$Ro\left(\frac{\partial u'_1}{\partial t} + u'_0 \frac{\partial u'_1}{\partial x} + v'_0 \frac{\partial u'_1}{\partial y} + w'_1 \frac{\partial u'_0}{\partial z}\right) - v'_1 + \frac{Ro\Pi}{\rho'_0} \frac{\partial p'_1}{\partial x} - \frac{K_m}{fH^2} \frac{\partial^2 u'_1}{\partial z^2} = 0,$$

$$Ro\left(\frac{\partial v'_1}{\partial t} + u'_0 \frac{\partial v'_1}{\partial x} + v'_0 \frac{\partial v'_1}{\partial y} + w'_1 \frac{\partial v'_0}{\partial z}\right) + u'_1 + \frac{Ro\Pi}{\rho'_0} \frac{\partial p'_1}{\partial y} - \frac{K_m}{fH^2} \frac{\partial^2 v'_1}{\partial z^2} = 0,$$

$$\frac{\Pi}{\rho'_0} \frac{\partial p'_1}{\partial z} - \frac{\rho'_1}{\rho'_0} \frac{\Pi}{\rho'_0} \frac{\partial p'_0}{\partial z} = \frac{\Pi}{\rho'_0} \frac{\partial p_1}{\partial z} + \frac{\rho'_1}{\rho'_0} g_0 = 0,$$

$$\frac{\partial u_1'}{\partial x} + \frac{\partial v_1'}{\partial y} + \frac{\partial w_1'}{\partial z} = 0, \quad (27)$$

$$\frac{P}{\rho \Theta R} p_1' = \rho_o' T_1' + T_o' \rho_1',$$

$$\text{Ro} \left[ \frac{\partial T_1'}{\partial t} + u_o' \frac{\partial T_1'}{\partial x} + v_o' \frac{\partial T_1'}{\partial y} + w_1' \left( \frac{\partial T_o'}{\partial z} + \frac{g}{C_p} \frac{H}{\Theta} \right) \right] - \frac{K_m}{fH^2 \text{Pr}} \frac{\partial^2 T_1'}{\partial z^2} = 0.$$

A consequence of the Boussinesq approximation as shown by Spiegel and Veronis (1960) is

$$\frac{\rho_1'}{\rho_o'} + \frac{T_1'}{T_o'} \approx 0. \quad (27a)$$

This is substituted into the vertical momentum equation to give

$$\frac{\Pi}{\rho_o'} \frac{\partial p_1'}{\partial z} - \frac{T_1'}{T_o'} g_o = 0. \quad (27b)$$

It will now be assumed that the structure of the instability is two dimensional such that along the x axis,  $\frac{\partial(\ )_1}{\partial x} = 0$ . The coordinate transformation is a rotation by an angle  $\epsilon$  from  $\mathcal{V}_g$  (see Fig. 1). Eqs. (27, 27b) become then

$$\begin{aligned} \text{Ro} \left( \frac{\partial u_1}{\partial t} + v_o \frac{\partial u_1}{\partial y} + w_1 \frac{\partial u_o}{\partial z} \right) - v_1 - \frac{K_m}{fH^2} \frac{\partial^2 u_1}{\partial z^2} &= 0, \\ \text{Ro} \left( \frac{\partial v_1}{\partial t} + v_o \frac{\partial v_1}{\partial y} + w_1 \frac{\partial v_o}{\partial z} \right) + u_1 + \frac{\Pi \text{Ro}}{\rho_o} \frac{\partial p_1}{\partial y} - \frac{K_m}{fH^2} \frac{\partial^2 v_1}{\partial z^2} &= 0, \\ \frac{\Pi}{\rho_o} \frac{\partial p_1}{\partial z} - \frac{T_1}{T_o} g_o &= 0, \\ \frac{\partial v_1}{\partial y} + \frac{\partial w_1}{\partial z} &= 0, \end{aligned} \quad (28)$$

$$\text{Ro} \left[ \frac{\partial T_1}{\partial t} + v_o \frac{\partial T_1}{\partial y} + w_1 \left( \frac{\partial T_o}{\partial z} + \frac{g}{C_p} \frac{H}{\Theta} \right) \right] - \frac{K_m}{fH^2 \text{Pr}} \frac{\partial^2 T_1}{\partial z^2} = 0 .$$

The solutions to the zero order equations in the new coordinates are

$$\begin{aligned} u_o &= u'_o \cos \epsilon + v'_o \sin \epsilon , \\ v_o &= -v'_o \sin \epsilon + v'_o \cos \epsilon . \end{aligned} \tag{29}$$

The assumption of the two-dimensional structure is made on the basis that the inflection point instability occurs in plane parallel flow (Lin, 1945). Also, observations of inflection point instability in laboratory fluid flow experiments show a two-dimensional structure to the instability waves (Faller and Kaylor, 1966).

A number of terms in the boundary layer equations (17) do not appear in (28) because they are of a higher order in  $\chi$ . The degree to which they are actually smaller in magnitude depends on how much less than one is  $\chi$ . The smaller effects generated by these higher order terms can be included in the stability analysis by adding these terms to (28) with powers of  $\chi$  as their coefficients. Eq. 28 then becomes

$$\begin{aligned} \frac{\partial u_1}{\partial t} + v_o \frac{\partial u_1}{\partial y} + w_1 \frac{\partial u_o}{\partial z} - \frac{v_1}{\text{Ro}} - \frac{\chi}{\text{Re}} \frac{\partial^2 u_1}{\partial y^2} - \frac{1}{\text{Re}\chi} \frac{\partial^2 u_1}{\partial z^2} &= 0, \\ \frac{\partial v_1}{\partial t} + v_o \frac{\partial v_1}{\partial y} + w_1 \frac{\partial v_o}{\partial z} + \frac{u_1}{\text{Ro}} + \frac{\Pi}{\rho_o} \frac{\partial p_1}{\partial y} - \frac{\chi}{\text{Re}} \frac{\partial^2 v_1}{\partial y^2} - \frac{1}{\text{Re}\chi} \frac{\partial^2 v_1}{\partial z^2} &= 0, \\ \chi^2 \left( \frac{\partial w_1}{\partial t} + v_o \frac{\partial w_1}{\partial y} \right) + \frac{\Pi}{\rho_o} \frac{\partial p_1}{\partial z} - \frac{T_1}{T_o} g_o - \frac{\chi^3}{\text{Re}} \frac{\partial^2 w_1}{\partial y^2} - \frac{\chi}{\text{Re}} \frac{\partial^2 w_1}{\partial z^2} &= 0, \end{aligned} \tag{30}$$

$$\frac{\partial v_1}{\partial y} + \frac{\partial w_1}{\partial z} = 0 ,$$

$$\frac{\partial T_1}{\partial t} + v_o \frac{\partial T_1}{\partial y} + w_1 \frac{\partial \theta}{\partial z} - \frac{\chi}{\text{RePr}} \frac{\partial^2 T_1}{\partial y^2} - \frac{1}{\text{Re}\chi\text{Pr}} \frac{\partial^2 T_1}{\partial z^2} = 0,$$

where

$$\frac{\partial \theta}{\partial z} = \left( \frac{\partial T_o}{\partial z} + \frac{g}{C_p} \frac{H}{\Theta} \right).$$

An investigation by Lilly (1966) shows as  $Ro$  increases the coupling between the  $u$  and  $v$  momentum equations via the Coriolis force becomes unimportant to the Ekman layer instability. When the inflection point instability dominates at large Reynolds numbers, the  $u$  momentum equation can be neglected. Since  $\chi\text{Re} = 2Ro$ , the magnitude of the Coriolis terms and the vertical eddy transport terms are of the same order. Their physical contribution to the instability problem are different, however. The eddy viscous terms become important at the boundaries and at the critical layer where the phase speed of the instability and that of the mean wind speed become equal. In addition, the eddy viscous terms are the most highly differentiated terms. For these reasons the Coriolis terms will be dropped from (30), but the eddy viscous terms retained. The set of equations for the inflection point instability model in a stratified atmosphere are

$$\begin{aligned} \frac{\partial v_1}{\partial t} + v_o \frac{\partial v_1}{\partial y} + w_1 \frac{\partial v_o}{\partial z} + \frac{\Pi}{\rho_o} \frac{\partial p_1}{\partial y} - \frac{\chi}{\text{Re}} \frac{\partial^2 v_1}{\partial y^2} - \frac{1}{\text{Re}\chi} \frac{\partial^2 v_1}{\partial z^2} &= 0, \\ \chi^2 \left( \frac{\partial w_1}{\partial t} + v_o \frac{\partial w_1}{\partial y} \right) + \frac{\Pi}{\rho_o} \frac{\partial p_1}{\partial z} - \frac{T_1}{T_o} g_o - \frac{\chi^3}{\text{Re}} \frac{\partial^2 w_1}{\partial y^2} - \frac{\chi}{\text{Re}} \frac{\partial^2 w_1}{\partial z^2} &= 0, \\ \frac{\partial v_1}{\partial y} + \frac{\partial w_1}{\partial z} &= 0, \end{aligned} \quad (31)$$

$$\frac{\partial T_1}{\partial t} + v_o \frac{\partial T_1}{\partial y} + w_1 \frac{\partial \theta}{\partial z} - \frac{\chi}{\text{RePr}} \frac{\partial^2 T_1}{\partial y^2} - \frac{1}{\text{Re}\chi\text{Pr}} \frac{\partial^2 T_1}{\partial z^2} = 0.$$

From the tower data it is possible to determine all of the coefficients of the  $v_1$ ,  $w_1$ , and  $T_1$  terms of (31). Cross-differentiation and subtraction will eliminate pressure from the equations. Then (31) becomes a set of linear partial differential equations. Various simplifications of this set of equations are possible depending upon the values of  $X$  and  $Re$ . For  $X$  close to one, the magnitude of  $Re$  determines how much smaller the eddy transport terms are compared to the acceleration and pressure terms. As  $Re \rightarrow \infty$  the problem reduces to the stratified Rayleigh stability equation. This equation possesses singularities, however.

As  $X$  becomes smaller, the modeled physical structure changes from symmetrical dimensions to a structure with a much larger horizontal extent compared to its depth. This would be appropriate to boundary layer phenomena that are restricted in the vertical direction by stable regions or wind shear regions. The effect on (31) is to increase the importance of the vertical eddy transport terms and to decrease the vertical acceleration. The horizontal eddy transport terms are smaller than the vertical eddy terms by a factor of  $X^2$ . These conclusions can be verified from the locus of the most unstable perturbation found in a linear perturbation analysis by Brown (1972a) of a set of equations similar to (31). The coefficients of the vertical velocity terms are found to be 0.25 the value of the horizontal velocity terms, and the horizontal eddy terms are 0.25 the value of the vertical eddy terms.

Brown (1970) finds that for a neutral atmosphere the model produces an equilibrium flow consisting of a modified Ekman spiral plus a helical secondary flow. He speculates that for a stable atmosphere it might be possible for the Ekman spiral to develop. With warming producing

an adiabatic region in the lower levels, the inflection point instability could begin to operate when the less stable air reached the inflection point height. It appears that this is the case seen in the tower data. The scaling indicates small vertical accelerations which would inhibit large growing unstable perturbations. The instability should be limited to the incipient stage of the instability mode. The turbulence generated would have a small vertical scale.

With the form of the continuity equation in (31), the velocity components can be written in terms of a streamfunction, i.e.,  $v_1 = \partial\psi/\partial z$ ,  $w_1 = -\partial\psi/\partial y$ . Pressure may be eliminated from this set of equations by cross-differentiation and subtraction of the  $v_1$  and  $w_1$  momentum equations. From the zero-order set of equations, solutions are known for  $v_0$  and  $T_0$ . The non-dimensional parameters may be specified from the tower data. A linear perturbation analysis of the inflection point instability can be done by assuming the streamfunction and temperature are specified as simple-harmonic perturbations of the form

$$\begin{aligned}\Psi &= \varphi \exp [i \alpha(y - ct)] , \\ T_1 &= \tau \exp [i \alpha(y - ct)] .\end{aligned}\tag{32}$$

The wavenumber is  $\alpha$  and  $c$  is the complex phase speed,  $c = c_r + i c_i$ .  $\varphi$  and  $\tau$  are functions of  $z$ . Substitution of (32) into (31) results in the following set of perturbation differential equations

$$\begin{aligned}i \alpha \chi \operatorname{Re} \{ (v_0 - c) \left[ \frac{\partial^2 \varphi}{\partial z^2} - \alpha^2 \chi^2 \varphi \right] - \frac{\partial^2 v_0}{\partial z^2} \varphi \} \\ - \frac{\partial^4 \varphi}{\partial z^4} + 2 \alpha^2 \chi^2 \frac{\partial^2 \varphi}{\partial z^2} - \alpha^4 \chi^4 \varphi + \frac{g_0}{T_0} \tau = 0 , \\ i \alpha \chi \operatorname{RePr} \{ (v_0 - c) \tau - \frac{\partial \theta}{\partial z} \varphi \} - \frac{\partial^2 \tau}{\partial z^2} + \alpha^2 \chi^2 \tau = 0 .\end{aligned}\tag{33}$$

It is possible to arrange this set as a single sixth-order differential equation in  $\varphi$ . It is

$$\begin{aligned}
& \frac{\partial^6 \varphi}{\partial z^6} - [3 \alpha^2 \chi^2 + i \alpha \chi \text{Re} (v_0 - c)(1 + \text{Pr})] \frac{\partial^4 \varphi}{\partial z^4} \\
& - 2 i \alpha \chi \text{Re} \frac{\partial v_0}{\partial z} \frac{\partial^3 \varphi}{\partial z^3} + [3 \alpha^4 \chi^4 + 2 i \alpha^3 \chi^3 \text{Re} (v_0 - c) (1 + \text{Pr}) \\
& - \alpha^2 \chi^2 \text{Re}^2 \text{Pr} (v_0 - c)^2] \frac{\partial^2 \varphi}{\partial z^2} + 2 i \alpha \chi \text{Re} \left[ \frac{\partial^3 v_0}{\partial z^3} + \alpha^2 \chi^2 \frac{\partial v_0}{\partial z} \right] \frac{\partial \varphi}{\partial z} \\
& + [ \alpha^6 \chi^6 + i \alpha \chi \text{Re} \frac{\partial^4 v_0}{\partial z^4} - i \alpha^5 \chi^5 \text{Re} (v_0 - c) (1 + \text{Pr}) \\
& + \alpha^2 \chi^2 \text{Re}^2 \text{Pr} \frac{\partial^2 v_0}{\partial z^2} (v_0 - c) + \alpha^4 \chi^4 \text{Re}^2 \text{Pr} (v_0 - c)^2 \\
& - \alpha^2 \chi^2 \text{Re}^2 \text{Pr} \text{Ri}_b ] \varphi = 0 .
\end{aligned} \tag{34}$$

This constitutes an eigenvalue problem where  $c$  is the complex eigenvalue and  $\varphi$  is the eigenfunction. The boundary conditions are set at  $z = 0$  and at some height  $H'$ . The boundary conditions chosen for the cases here are  $v_1 = w_1 = T_1 = 0$  at  $z = 0$  and  $z = H'$ . In terms of  $\varphi$  these boundary conditions are

$$\varphi(0) = \frac{\partial \varphi}{\partial z}(0) = 0,$$

$$\frac{\partial^4 \varphi}{\partial z^4}(0) + [i \alpha \chi \text{Re} c - 2 \alpha^2 \chi^2] \frac{\partial^2 \varphi}{\partial z^2}(0) = 0, \tag{35}$$

and

$$\varphi(H') = \frac{\partial \varphi}{\partial z}(H') = 0,$$

(36)

$$\frac{\partial^4 \varphi}{\partial z^4}(H') + [i \alpha \chi \text{Re} (c - v_0(H')) - 2 \alpha^2 \chi^2] \frac{\partial^2 \varphi}{\partial z^2}(H') = 0 .$$

From the data are obtained the values of  $\alpha$ ,  $\chi$ ,  $Re$ ,  $Pr$  and  $Ri_b$ . The Ekman solutions with knowledge of  $\underline{v}_g$  and  $\delta$  provides values of  $v_o$  and its derivatives. Eq. (34) with boundary conditions (35) and (36) is solved for the eigenvalue  $c$ . The perturbations will grow in amplitude with time for a positive  $c_i$ . Thus inflection point instability is revealed when the solution is  $c_i > 0$ . The method employed to solve (34), (35) and (36) is the "shooting method". It is described in the appendix. The next chapter gives the result of using the tower measured data in this instability model.

## CHAPTER VII

### COMPARISON OF THE DATA AND THE INFLECTION POINT INSTABILITY MODEL

Confidence in the inflection point instability as the source of the turbulent temperature fluctuations will be acquired if input of the tower data and estimates of parameters from the tower data into the model produces unstable perturbations. The model parameters are calculated from the data and then (34) is solved for  $c$ . The linear perturbation model indicates instability when  $c_i$  is greater than zero. It is believed, because of the strong damping expected in the highly stable regions of the inversion, that fully developed finite-amplitude perturbation flows will not develop. The incipient instability predicted by the infinitesimal perturbation analysis should then be adequate for the explanation of the observed temperature fluctuations.

In Chapter IV were determined the model parameters  $Re$  and  $Ri$ . The specification of  $v_0$  and its derivatives depend upon  $\delta$ ,  $V_g$  and  $\epsilon$ . These also have been tabulated in that section. The Prandtl number has been set at a constant 1.0. The limits of the integration are from  $z = 0$  to  $z = H' = 6\delta$ . The parameters  $\alpha$  and  $\chi$  are determined from  $\delta$  and the estimated wavelengths which are functions of  $\epsilon$ . The product

$$\alpha \chi = \frac{2 \pi \delta}{\lambda} = \alpha^*$$

can be calculated from the values of  $\delta$  and  $\lambda$ . It has been listed in Tables 4 and 5 along with the other parameters. It is possible now to

calculate values of  $c_i$  and find whether the model produces the inflection point instability, given input from the tower data.

The growth rate in terms of  $V_g$  and  $\delta$  is  $\alpha^*c_i$ . These have been listed in Table 4 at 0800 CST on 25 October and in Table 5 at 0730 CST on 28 October. The locus of the largest positive growth rate at 0800 CST, 25 October 1971, is at a wavenumber  $0.436/\delta$  and  $\epsilon$  of  $35^\circ$ . On 28 October 1971, 0730 CST, it is at  $\alpha^* = 0.554/\delta$  and  $\epsilon$  is  $35^\circ$ .

Results from Brown (1972a) and this study show that the inflection point instability is completely damped,  $c_i < 0.0$ , for  $Ri_b > 0.02$ . On 25 October the temperature fluctuations are not present at 0700 CST when all  $Ri_b$  are greater than 0.02, but have started at 0730 CST when some of the  $Ri_b$  are less than 0.02. For fixed values of  $Re$  and  $Ri_b$ , Brown (1972a) has searched the  $\epsilon$  and  $\alpha^*$  domain for the locus of the maximum positive growth rate. Additional computations were completed for this study to better define this locus in the stable region. Fig. 15 shows values of growth rate,  $\alpha^*c_i$ , in the  $\epsilon$  and  $\alpha^*$  domain. It shows that at the locus of maximum  $\alpha^*c_i$ ,  $\epsilon$  changes from  $20^\circ$  at  $Ri_b = 0.0$ , to  $35^\circ$  at  $Ri_b = 0.018$ . The wavenumber,  $\alpha^*$ , changes from  $0.5/\delta$  at  $Ri_b = 0.0$ , to  $0.43/\delta$  at  $Ri_b = 0.018$ . Thus, the results obtained from the tower data agree well with the values of  $\epsilon$  and  $\alpha^*$  expected for the incipient instability at  $Ri_b$  close to 0.02. The uncertainties in determining  $\lambda$  from the data could easily account for the variation in  $\alpha^*$  at the maximum growth rate.

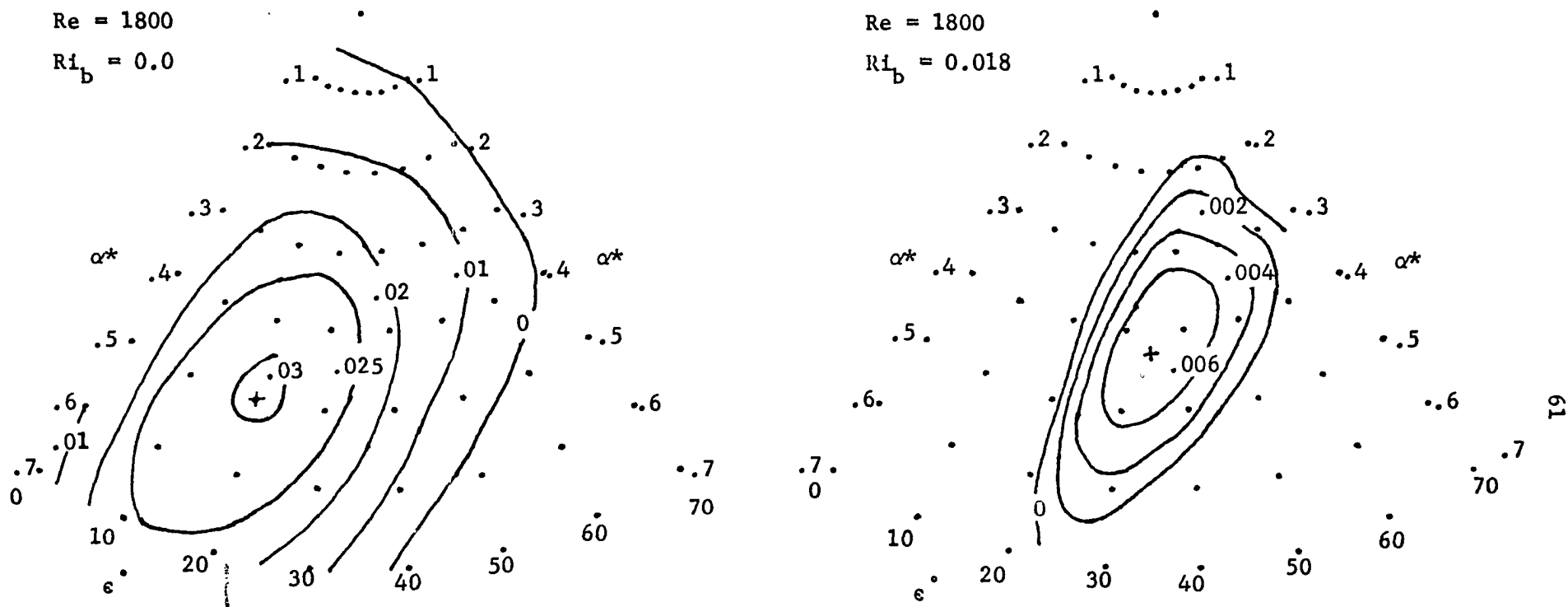


Figure 15. Values of the growth rate,  $\alpha^*c_i$ . Units of  $\alpha^*c_i$  are  $V_g/\delta$ , those of  $\alpha^*$  are  $1/\delta$ . The figure shows how the locus of maximum growth rate, indicated by +, changes as  $Ri_b$  changes from 0.0 to 0.018. It also shows that as  $Ri_b$  increases the value of the growth rate decreases.

## CHAPTER VIII

### CONCLUSION

Observed in the tower data are temperature fluctuations which occur near the inflection point in the wind profile. It is suggested that the inflection point instability mechanism is responsible for these temperature fluctuations. Here is how it might occur. An Ekman wind profile develops within the stable stratification of the nocturnal inversion. After sunrise the small-scale surface-layer turbulence creates an adiabatic region near the heated earth. As time passes and more heat is added, the depth of this adiabatic region increases. The transition layer between the adiabatic layer and the inversion region moves upward. As the transition layer encounters the inflection point in the wind profile, the Richardson number at the inflection point begins to decrease. When the Richardson number falls below a certain value, the inflection point instability mechanism begins to operate. The instability occurs as small-scale turbulence which is severely damped. Further upward movement of the transition layer alters the wind profile such that the height of the inflection point also rises. Thus, the inflection point continues to be within a stable region and the instability remains in an incipient state. This incipient state is characterized by the large value of  $\epsilon$  and is confined to a shallow layer.

The presence of the instability appears to have some effect on the rate of dissipation of the nocturnal inversion. Because of the fog,

the rate of heating at the earth's surface on 28 October 1971 is less than the heating rate on 25 October 1971. However, on both mornings the inversion dissipated at about the same rate. The transition to a super-adiabatic boundary layer was delayed three to four hours over the transition period on 25 October. It seems the instability could have a considerable contribution to the mixing process at the inversion base and the subsequent dissipation of the inversion. The inversion behavior model shows a large contribution from the breaking wave parameterization on 25 and 28 October.

The other Ekman layer instabilities, i.e., convective, parallel and resonance, do not resemble the observed boundary layer structure as well as the inflection point instability model does. The distinction between other instability mechanisms and the inflection point mechanism cannot be completely resolved with the single tower and 90 m spacing of the measurement levels. To do this it would be necessary to observe the fine structure of the temperature and the three-dimensional velocity components. It is possible however, to compare some aspects of the tower data and the instability model. The resemblance is quite good of the observed mean wind profile to the Ekman spiral which is the mean wind profile of the model. For the perturbation quantities, wind and temperature data measured on the meteorological tower have been used to derive input parameters to a linear infinitesimal perturbation model of the inflection point instability mechanism. The perturbations have positive growth rates and so indicate instability for certain values of the input data. Based on the largest positive growth rate, the instability is oriented  $35^\circ$  to the left of the geostrophic wind and has a wavenumber of  $0.44/\delta$  on 25 October and  $0.55/\delta$  on 28 October. Another

parameter of the model is the aspect ratio. This is tabulated in Table 7. The magnitude of  $\chi$  at the orientation angle associated with the maximum positive growth rate of the perturbation is 0.14 on 25 October and 0.18 on 28 October. This result confirms the small parameter assumption in Chapter VI.

TABLE 7  
ASPECT RATIO FOR DIFFERENT VALUES OF  $\epsilon$

Date	Time	$\epsilon$	$\chi$
25 October 1971	0800	20°	0.3774
		25°	0.2398
		30°	0.1764
		35°	0.1388
		40°	0.1158
		45°	0.1008
		50°	0.0891
		55°	0.0806
28 October 1971	0730	20°	0.4997
		25°	0.3011
		30°	0.2228
		35°	0.1763
		40°	0.1477
		45°	0.1267
		50°	0.1117
		55°	0.1009
		60°	0.0920

The value of this analysis of the tower data is to show the validity of the Ekman layer model to an atmospheric boundary layer problem. The lack of observations of the Ekman spiral has resulted in some neglect of its study. This application of the inflection point instability model to the observed tower data supports the idea of an Ekman transition layer during the dissipation of a morning inversion. The model of inversion dynamics shows a contribution of this wind shear instability in some cases to the dissipation of the nocturnally formed surface inversion.

## REFERENCES

- Asai, T., and I. Nakasuji, 1973: On the stability of Ekman boundary layer flow with thermally unstable stratification. J. Meteor. Soc. Japan, 48, 29-42.
- Betts, A. K., 1973: Non-precipitating cumulus convection and its parameterization. Quart. J. Roy. Meteor. Soc., 99, 178-196.
- \_\_\_\_\_, 1974: Reply to comment on the paper 'Non-precipitating cumulus convection and its parameterization'. Quart. J. Roy. Meteor. Soc., 100, 469-471.
- Blackadar, A. K., 1957: Boundary layer wind maxima and their significance to the growth of nocturnal inversions. Bull. Amer. Meteor. Soc., 38, 283-290.
- Brown, R. A., 1970: A secondary flow model of the planetary boundary layer. J. Atmos. Sci., 27, 742-757.
- \_\_\_\_\_, 1972a: On the inflection point instability of a stratified Ekman boundary layer. J. Atmos. Sci., 29, 850-859.
- \_\_\_\_\_, 1972b: On the physical mechanism of the inflection point instability. J. Atmos. Sci., 29, 984-986.
- \_\_\_\_\_, and F. Lee, 1972: On the shooting method applied to the rotating stratified boundary layer stability problem. J. Comput. Phys., 10, 107-122.
- Carson, D. J., 1973: The development of a dry inversion-capped convective unstable boundary layer. Quart. J. Roy. Meteor. Soc., 99, 450-467.
- Carter, J. K., 1970: The meteorologically instrumented WKY-TV tower facility. NOAA Tech. Memo. ERTLM-NSSL-50, 57 pp.
- Conte, S. D., 1966: The numerical solution of linear boundary value problems. SIAM Rev., 8, 299-321.
- Deardorff, J. W., G. E. Willis, and D. K. Lilly, 1969: Laboratory investigation of non-steady penetrative convection. J. Fluid Mech., 37, 643-665.
- Emmanuel, C. B., B. R. Bean, L. G. McAllister and J. R. Pollard, 1972: Observations of Helmholtz waves in the lower atmosphere with an acoustic sounder. J. Atmos. Sci., 29, 886-892.

- Faller, A. J., and R. E. Kaylor, 1966: A numerical study of the laminar Ekman layer. J. Atmos. Sci., 23, 466-480.
- Gersting, J. M., 1970: Computer Programs for the Analysis of Certain Problems in Hydrodynamic Stability. Arizona State University Engineering Report.
- Hanafusa, T., 1971: A new method of on-site analysis of turbulent transports near the ground. Contributions of Geophysical Inst., Kyoto University, 11, 33-45.
- Hardy, K. R., 1972: Studies of the clear atmosphere using high power radar. Remote Sensing of the Troposphere, V. E. Derr, Ed., Washington, D.C., Government Printing Office, Chapter 14.
- Kaylor, R. E., and A. J. Faller, 1972: Instability of the stratified Ekman boundary layer and the generation of internal waves. J. Atmos. Sci., 29, 497-509.
- LeMone, M. A., 1973: The structure and dynamics of horizontal roll vortices in the planetary boundary layer. J. Atmos. Sci., 30, 1077-1091.
- Lilly, D. K., 1966: On the stability of Ekman boundary flow. J. Atmos. Sci., 23, 481-494.
- Lin, C. C., 1945: On the stability of two-dimensional parallel flows. Part II. Quart. Appl. Math., 3, 218-234.
- Sanders, L. D., and A. H. Weber, 1970: Evaluation of roughness length at the NSSL-WKY meteorological tower. NOAA Tech. Memo. ERL-NSSL-57, 24 pp.
- Spiegel, E. A., and C. Veronis, 1960: On the Boussinesq approximation for a compressible fluid. Astrophys. J., 131, 442-447.
- Tennekes, H., 1973: A model for the dynamics of the inversion above a convective boundary layer. J. Atmos. Sci., 30, 558-567.
- \_\_\_\_\_, 1974: Short-term forecasts of temperature and mixing height on sunny days. Preprints Symposium on Atmospheric Diffusion and Air Pollution. Santa Barbara, American Meteorological Society, 35-40.

## APPENDIX

This section describes the numerical method used to solve the differential eigenvalue problem (34). It is known as the "shooting method" and is the same method used by Brown (1972a) and Brown and Lee (1972).

The procedure is to first estimate the eigenvalue,  $c$ . With this estimate the problem becomes a linear boundary value problem. The  $n$ -th-order differential equation can be written as a system of first order differential equations, e.g.,

$$\frac{d\tilde{\phi}}{dz} = \underline{A}(z)\tilde{\phi}, \text{ where } \tilde{\phi} = \begin{bmatrix} \phi \\ \frac{\partial \phi}{\partial z} \\ \cdot \\ \cdot \\ \frac{\partial^n \phi}{\partial z^n} \end{bmatrix}, \quad (\text{A1})$$

and  $\underline{A}$  is the  $n \times n$  matrix containing the coefficients of the differential equations.

The general solution to the linear boundary value problem of  $n$ -th-order with  $k$  boundary conditions at the inner boundary is a superposition of  $k$  linearly independent solutions, i.e.,

$$\varphi(z) = \beta_1 \varphi(1) + \beta_2 \varphi(2) + \dots + \beta_k \varphi(k) \quad (\text{A2})$$

The  $\beta$ 's are chosen so as to satisfy the inner boundary conditions. The linear boundary value problem is now written as

$$\frac{d\underline{Y}}{dz} = \underline{A}(z) \underline{Y}, \quad (\text{A3})$$

$$\underline{B} \underline{Y}(0) = 0, \quad (\text{A4})$$

$$\underline{D} \underline{Y}(H') = 0, \quad (\text{A5})$$

where

$$Y = \begin{bmatrix} \varphi(1) & \varphi(2) & \cdots & \varphi(k) \\ \frac{\partial \varphi(1)}{\partial z} & & & \cdot \\ \cdot & & & \cdot \\ \cdot & & & \cdot \\ \frac{\partial^n \varphi(1)}{\partial z^n} & \cdot & \cdot & \frac{\partial^n \varphi(k)}{\partial z^n} \end{bmatrix}.$$

$\underline{D}$  is a  $(n-k) \times n$  matrix and  $\underline{B}$  is a  $k \times n$  matrix. Eq. (A4) is the inner boundary condition and (A5) is the outer boundary condition. To solve this linear boundary value problem, initial values of  $\underline{Y}$  are chosen so as to satisfy the outer boundary condition, i.e., satisfy (A5). Eq. (A3) is integrated from the outer boundary to the inner boundary. At the inner boundary the  $\beta$ 's are found by requiring

$$\underline{B} \underline{Y}(0) \begin{bmatrix} \beta_1 \\ \beta_2 \\ \cdot \\ \cdot \\ \beta_k \end{bmatrix} = 0. \quad (\text{A6})$$

For this to be true the determinant of the coefficient of  $\beta$ 's must vanish,

i.e.,

$$|\underline{B} \underline{Y}(0)| = f(c) = 0. \quad (\text{A7})$$

Remember, however,  $c$  was estimated, therefore the determinant will not

vanish unless the guess was correct. Eq. (A7) sets up a functional relationship between  $c$  and the condition that the determinant vanish. Then  $c$  is found by determining the roots of the function  $f(c)$ . This is an iterative procedure where  $c$  is estimated, then the estimate is refined until the inner boundary condition is satisfied.

Initially the columns of  $\underline{y}$  are orthogonal. As the integration proceeds, however, errors due to the finite arithmetic of the computer will cause rapidly growing errors to accumulate and the solutions will no longer remain independent. If this were allowed to continue the solution at the inner boundary would be meaningless. To overcome this problem a method of near-orthonormalization developed by Conte (1966) is used. A check is made at each step of the integration and if the vectors

$$\underline{y}(i) = \begin{bmatrix} \varphi(i) \\ \frac{\partial \varphi(i)}{\partial z} \\ \cdot \\ \cdot \\ \frac{\partial^n \varphi(i)}{\partial z^n} \end{bmatrix}, \quad i = 1, \dots, k, \quad (\text{A8})$$

meet certain non-orthogonality conditions, they are orthonormalized.

The Gram-Schmidt recursion formulas for orthonormalizing a set of vectors  $\underline{\tilde{\phi}}(1), \dots, \underline{\tilde{\phi}}(k)$  follows:

$$\langle \underline{\tilde{\phi}}(1), \underline{\tilde{\phi}}(1) \rangle = \sum_{j=0}^n \varphi_{(1)}^j \cdot \bar{\varphi}_{(1)}^j, \quad (\text{A9})$$

where  $(\tilde{\Phi}(1), \tilde{\Phi}(1))$  is the complex scalar product,  $\bar{\Phi}(1)^j$  is the complex conjugate of the  $j$ -th derivative of the first independent solution;

$$\begin{aligned} \tilde{W}_{11} &= (\tilde{\Phi}(1), \tilde{\Phi}(1))^{\frac{1}{2}}, & \tilde{Z}(1) &= \frac{\tilde{\Phi}(1)}{\tilde{W}_{11}}, \\ \tilde{X}(2) &= \tilde{\Phi}(2) - (\tilde{\Phi}(2), \tilde{Z}(1))\tilde{Z}(1), & \tilde{W}_{22} &= (\tilde{\Phi}(2), \tilde{\Phi}(2))^{\frac{1}{2}}, \\ \tilde{Z}(2) &= \frac{\tilde{X}(2)}{\tilde{W}_{22}}, & i &= 1, \dots, k, \\ \tilde{X}(i) &= \tilde{\Phi}(i) - (\tilde{\Phi}(i), \tilde{Z}(1))\tilde{Z}(1) - \dots - (\tilde{\Phi}(i), \tilde{Z}(i-1))\tilde{Z}(i-1), \\ \tilde{W}_{ii} &= (\tilde{\Phi}(i), \tilde{\Phi}(i))^{\frac{1}{2}}, & \tilde{Z}(i) &= \frac{\tilde{X}(i)}{\tilde{W}_{ii}}. \end{aligned} \tag{A10}$$

The  $\tilde{Z}(i)$  are the orthonormalized vectors that are the initial conditions for the next step of the integration.

The criteria for determining if it is necessary to orthonormalize the vectors  $\tilde{\Phi}(i)$ , is to determine the angle between the vectors and to orthonormalize when any of the angles become too small. This criteria can be written as

$$\min_{(i,j)} \left\{ \cos^{-1} \left| \frac{(\tilde{\Phi}(i), \tilde{\Phi}(j))}{[(\tilde{\Phi}(i), \tilde{\Phi}(i))(\tilde{\Phi}(j), \tilde{\Phi}(j))]^{\frac{1}{2}}} \right| \right\} < \gamma', \quad \begin{array}{l} i, j = 1, \dots, k \\ i \neq j \end{array}. \tag{A11}$$

The angle  $\gamma'$  has a range,  $0^\circ \leq \gamma' \leq 90^\circ$ . For  $\gamma' = 90^\circ$  the orthonormalizations occur at each step of the integration. For less than  $90^\circ$ , computer time is saved while the parasitic error is still controlled. Generally there is an optimum  $\gamma'$ , but this facet of the method was not explored.

Now the procedure will be shown for the problem in this study.

The sixth order differential equation, (34), can be written as

$$\varphi^{vi} + c_1\varphi^v + c_2\varphi^{iv} + c_3\varphi^{iii} + c_4\varphi^{ii} + c_5\varphi^i + c_6\varphi = 0 \quad , \quad (A12)$$

where the superscripts indicate differentiation with respect to  $z$  and the  $c$ 's represent the coefficients of the differential equation. The boundary conditions at  $z = 0$  are,  $v_1 = w_1 = T_1 = 0$ . At  $z = H'$ , they are the same. The linear system of first order differential equations is  $y_1 = \varphi$ ,  $y_2 = \varphi^i$ ,  $y_3 = \varphi^{ii}$ ,  $y_4 = \varphi^{iii}$ ,  $y_5 = \varphi^{iv}$ ,  $y_6 = \varphi^v$ , and

$$\frac{d}{dz} \begin{bmatrix} y_1 \\ y_2 \\ y_3 \\ y_4 \\ y_5 \\ y_6 \end{bmatrix} = \begin{bmatrix} 0 & 1 & 0 & 0 & 0 & 0 \\ 0 & 0 & 1 & 0 & 0 & 0 \\ 0 & 0 & 0 & 1 & 0 & 0 \\ 0 & 0 & 0 & 0 & 1 & 0 \\ 0 & 0 & 0 & 0 & 0 & 1 \\ c_6 & c_5 & c_4 & c_3 & c_2 & c_1 \end{bmatrix} \begin{bmatrix} y_1 \\ y_2 \\ y_3 \\ y_4 \\ y_5 \\ y_6 \end{bmatrix} = \frac{d \underline{Y}}{dz} = \underline{A} \underline{Y} \quad . \quad (A13)$$

The boundary condition  $T(0) = 0$  and  $T(H') = 0$  can be written in term of  $\varphi$ . The sixth order equation reduces to

$$\varphi^{iv}(0) + b_1\varphi^{ii}(0) = 0 \quad , \quad \varphi^{iv}(H') + b_2\varphi^{ii}(H') = 0 \quad , \quad (A14)$$

at the boundaries. The boundary conditions in matrix form are

$$\begin{bmatrix} 1 & 0 & 0 & 0 & 0 & 0 \\ 0 & 1 & 0 & 0 & 0 & 0 \\ 0 & 0 & b_1 & 0 & 0 & 0 \end{bmatrix} \begin{bmatrix} y_1 \\ y_2 \\ y_3 \\ y_4 \\ y_5 \\ y_6 \end{bmatrix} = \underline{B} \underline{Y}(0) = 0 \quad , \quad (A15)$$

$$\begin{bmatrix} 1 & 0 & 0 & 0 & 0 & 0 \\ 0 & 1 & 0 & 0 & 0 & 0 \\ 0 & 0 & b_2 & 0 & 0 & 0 \end{bmatrix} \begin{bmatrix} y_1 \\ y_2 \\ y_3 \\ y_4 \\ y_5 \\ y_6 \end{bmatrix} = \underline{D} \underline{Y}(H') = 0 \quad . \quad (A16)$$

For this problem  $k = 3$  so that

$$\underline{Y} = \begin{bmatrix} y_1(1) & y_1(2) & y_1(3) \\ y_2(1) & y_2(2) & y_2(3) \\ y_3(1) & y_3(2) & y_3(3) \\ y_4(1) & y_4(2) & y_4(3) \\ y_5(1) & y_5(2) & y_5(3) \\ y_6(1) & y_6(2) & y_6(3) \end{bmatrix} . \quad (\text{A17})$$

The solution to (34) is then

$$\varphi(z) = \beta_1 y_1(1) + \beta_2 y_1(2) + \beta_3 y_1(3) , \quad (\text{A18})$$

where  $y_1(1)$ ,  $y_1(2)$ , and  $y_1(3)$  are found from solving

$$\begin{aligned} \frac{d \underline{Y}}{dz} &= \underline{A} \underline{Y} , \\ \underline{B} \underline{Y}(0) &= 0 , \\ \underline{D} \underline{Y}(H') &= 0 . \end{aligned} \quad (\text{A19})$$

Computer programs for the solution of the problem were adapted from Gersting (1970).